Estonian Journal of Earth Sciences
2025, **74**, 1, 61–82

https://doi.org/10.3176/earth.2025.05

www.eap.ee/earthsciences
Estonian Academy Publishers

RESEARCH ARTICLE

Received 13 August 2024
Accepted 11 November 2024
Available online 5 February 2025

Keywords:
Alutaguse zone, geochemistry, metasediments, metavolcanics, weathering and alteration indices, provenance, tectonic setting

Corresponding author:
Juan David Solano-Acosta
jusola@taltech.ee

Citation:
Solano-Acosta, J. D., Soesoo, A. and Hints, R. 2025. Geochemistry, provenance, and tectonic setting of Paleoproterozoic metasedimentary and metavolcanic units of the Estonian Alutaguse region, eastern Fennoscandia. *Estonian Journal of Earth Sciences*, **74**(1), 61–82. https://doi.org/10.3176/earth.2025.05

Geochemistry, provenance, and tectonic setting of Paleoproterozoic metasedimentary and metavolcanic units of the Estonian Alutaguse region, eastern Fennoscandia

Juan David Solano-Acosta[a], Alvar Soesoo[a,b,c] and Rutt Hints[a]

[a] Department of Geology, Tallinn University of Technology, Ehitajate tee 5, 19086 Tallinn, Estonia

[b] Geological Survey of Estonia, F. R. Kreutzwaldi 5, 44314 Rakvere, Estonia

[c] Department of Geology, University of Tartu, Ravila 14a, 50411 Tartu, Estonia

ABSTRACT

This research focuses on the geochemical analysis of Paleoproterozoic metasedimentary and metavolcanic units in the Alutaguse region of northern Estonia, shedding light on the geodynamic evolution during the Svecofennian orogeny in eastern Fennoscandia. The metasedimentary units consist of micaceous gneisses (± Grt ± Crd ± Sil), and the metavolcanic units include amphibolites and pyroxenic gneisses. Geochemical analyses utilized both historical and new whole-rock geochemical data. Weathering indices indicated their applicability for provenance studies and tectonic setting analyses. Metasediments are classified by their silica content: high-SiO_2 (>63 wt%) metasediments resemble litharenites, implying higher maturity and felsic origins akin to the upper continental crust reference; low-SiO_2 (<63 wt%) metasediments align with graywackes and shales, indicative of mafic to intermediate origins, similar to the post-Archean Australian shale, with TiO_2–Ni suggesting sedimentary trends. Discriminant tectonic parameters associated these metasedimentary groups with a continental rift domain. Total alkali-silica classified the metavolcanics as subalkaline units. Geochemical ratios, such as La/Yb vs. Zr/Nb and La/Sm vs. Sm/Yb, crossing the spinel-lherzolite trend, were closest to the primitive mantle reference. The Th/Nb and Th/Zr ratios revealed asthenospheric mantle origins for the basaltic magma sources in Alutaguse. Tectonic settings derived from Y/15–La/10–Nb/8 and TiO_2–10(MnO)–10(P_2O_5) ratios suggested a predominant oceanic arc affinity. It is proposed here that the Alutaguse structural zone developed as the back-arc of the Tallinn–Uusimaa belt(s), following the accretion of the Bergslagen microcontinent at 1.9–1.87 Ga, concluding with the closure of the paleo-Svecofennian ocean.

1. Introduction

The Estonian Paleoproterozoic crystalline basement in Baltica is not fully understood due to the predominance of Lower Paleozoic strata concealing it, with insights primarily derived from drill cores and geophysics (Puura and Huhma 1993; Kivisilla et al. 1999; Skridlaite and Motuza 2001; Soesoo et al. 2004; All et al. 2004; Bogdanova et al. 2015; Soesoo et al. 2020; Nirgi and Soesoo 2021; Solano-Acosta et al. 2023). Despite limited surface exposure, studies indicate high-grade Paleoproterozoic metavolcanic and metasedimentary rocks in northern Estonia, segmented principally into the Tallinn, Alutaguse, and Jõhvi structural zones (Fig. 1). These zones possess 1.92–1.88 Ga rocks, akin to those found in southwestern Finland and central Sweden's Bergslagen zone (Kirs et al. 2009; Bogdanova et al. 2015; Soesoo et al. 2020).

The Alutaguse zone has been described as a folded metasedimentary basin, formed post-closure of the Tallinn volcanic belt's back-arc, but it still lacks comprehensive geochemical and geochronological studies, making its evolutionary model unclear and its genesis widely debated (Kivisilla et al. 1999; Kirs et al. 2009; Bogdanova et al. 2015; Soesoo et al. 2020). Geophysical and isotopic studies suggest that the Tallinn zone is an accreted island arc belt, potentially extending into the Finnish southern Svecofennian Uusimaa belt domain across the Gulf of Finland seabed,

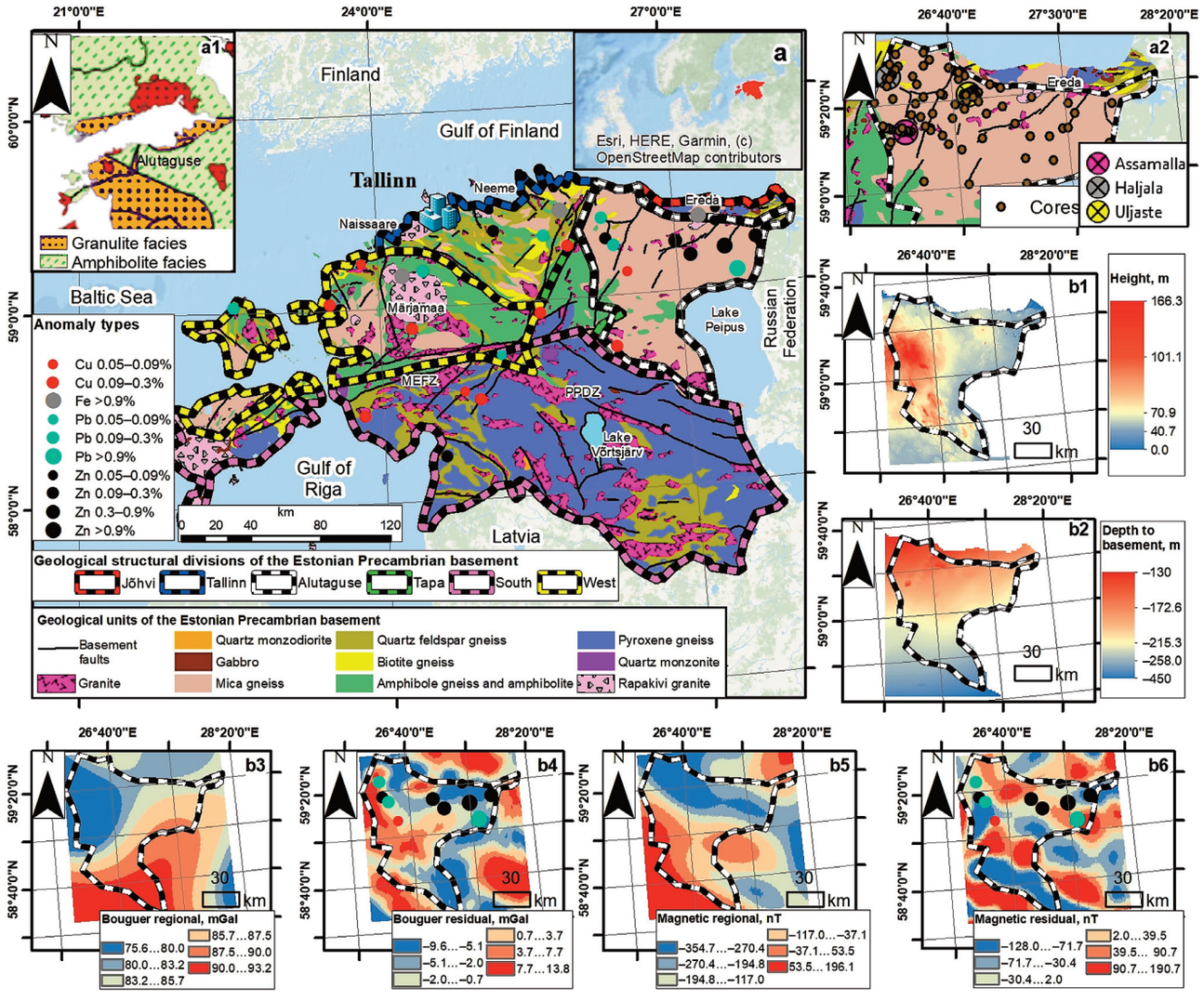

Fig. 1. **a** – geological schematic map of the Precambrian basement of Estonia, showing sulfide anomalies according to Soesoo et al. (2020); **a1** – inset illustrating the distribution of granulite- and amphibolite-facies metamorphic rocks, with reddish polygons corresponding to rapakivi lithologies, after Bogdanova et al. (2015); the anomaly types represent the most prominent metalliferous anomalies; **a2** – zoomed-in geological basement map of the Alutaguse zone, depicting the locations of cores and prominent metallogenic regions. **b** – geophysical maps of the Alutaguse zone, depicting the 10 × 10 m topography (**b1**), depth to basement (**b2**), Bouguer gravitational anomaly (**b3**), residual Bouguer anomaly (**b4**), regional magnetic anomaly (**b5**), and residual magnetic anomaly (**b6**). Residual maps present the locations of metalliferous anomalies. Graphs b3–b6 are modified after Solano-Acosta et al. (2023). The geological, topographical, and depth-to-basement data can be downloaded from the Geoportal of the Estonian Land Board. Abbreviations: MEFZ – Middle-Estonian fault zone, PPDZ – Åland–Paldiski–Pskov deformation zone.

implying that the Alutaguse zone may represent a back-arc extension of the Tallinn–Uusimaa belt(s) (Puura et al. 1983; Petersell and Levchenkov 1994; All et al. 2004; Kirs et al. 2009), with metamorphic alumino-gneisses dated to approximately 1.88 Ga (Kähkönen 2005; Bogdanova et al. 2015; Nironen 2017; Lahtinen et al. 2017; Kara et al. 2021).

The major, trace, and rare earth elements (REE) in metasediment and metavolcanic rocks provide insights into their origin, weathering processes, and tectonic settings, enhancing our understanding of crustal geochemistry (Bhatia and Crook 1986; McLennan et al. 1995; Han et al. 2019). These elements elucidate the contributions of felsic and mafic sources to crustal evolution and rock origin and provenance (Sifeta et al. 2005). Additionally, geochemical studies on Precambrian metasedimentary and metavolcanic units have been crucial in understanding ancient lithological arrangements within tectonic and geodynamic contexts (Lahtinen et al. 2002; Sifeta et al. 2005; Lahtinen et al. 2010; El-Bialy 2013; Chen et al. 2014; de Carvalho Mendes et al. 2021).

This research uses new and historical whole-rock data to present an updated geochemical analysis of the metasedimentary and metavolcanic rocks in the Alutaguse zone. The study focuses on analyzing major and trace elements, as well as REE components, to determine the composition and origin of the source rocks. The goal is to identify geochemical trends for weathering, depositional features, and tectonic settings, which can provide insights into the geodynamic evolution that shaped the Estonian Alutaguse zone. These patterns can provide insights into the processes that have shaped this area. Understanding these patterns enhances our knowledge of the geological development of the Svecofennian orogeny and the Proterozoic history of Estonia's basement within the broader

context of Fennoscandia (Kähkönen 2005; Kirs et al. 2009; Baltybaev 2013; Bogdanova et al. 2015; Nironen 2017; Soesoo et al. 2020; Pesonen et al. 2021; Kara 2021; Lahtinen et al. 2022).

2. Geological setting

The Estonian Paleoproterozoic crystalline basement, part of the 1.9–1.7 Ga old Svecofennian domain, features metasedimentary and metavolcanic rocks that underwent amphibolite-to-granulite metamorphism, with some retrograde modifications, associated with contemporaneous mafic to intermediate intrusions (Puura et al. 1983; Puura and Huhma 1993; Kivisilla et al. 1999; Soesoo et al. 2004; All et al. 2004; Kirs et al. 2009). Between 1.6–1.4 Ga, rapakivi granite plutons intruded the consolidated basement (All et al. 2004; Soesoo et al. 2020; Fig. 1a). Estonia's structural framework is outlined by the 30 km-wide northwest-trending Åland–PPDZ-MEFZ (Åland–Paldiski–Pskov deformation zone – Middle-Estonian fault zone) deformation zone, with major shear zones dipping 65–75° SSW, separating northern regions of amphibolite and granulite facies from predominantly granulitic southern regions (Puura et al. 1983; Soesoo et al. 2006; Kirs et al. 2009; Bogdanova et al. 2015; Soesoo et al. 2020; Solano-Acosta et al. 2023).

Geological categorization of Precambrian basement rocks in Estonia identifies three main age groups: (1) the oldest in northern Estonia, which includes amphibolite-facies metavolcanic rocks dated at 1918 ± 10 Ma (Petersell and Levchenkov 1994); (2) southern Estonia's granulitic metavolcanic rocks and tonalites in the Tapa zone, dated at 1832 ± 22, 1827 ± 7, and 1824 ± 26 Ma, and magnetite-rich gneisses in the Jõhvi zone with ages spanning 1874 ± 18 to 1789 ± 19 Ma (Soesoo et al. 2004, 2006; Kirs et al. 2009; Bogdanova et al. 2015; Soesoo et al. 2020); and (3) the youngest group, which includes 1.6 Ga rapakivi granite plutons and associated mafic and felsic rocks (Kirs and Petersell 1994; Soesoo and Hade 2012; Rämö et al. 2014). Notably, no dating analyses are reported for Alutaguse lithologies.

Northern Estonia's Svecofennian orogeny units host metamorphosed and migmatized amphibolite-facies rocks, divided into the Tallinn zone (northwest), which contains amphibolites and biotite-amphibole gneisses, and the Alutaguse zone (northeast), which presents high-alumina gneisses, amphibolites, and biotite-amphibole gneisses (Kivisilla et al. 1999; Soesoo et al. 2004; Kirs et al. 2009; Bogdanova et al. 2015). Additionally, the Jõhvi zone, located to the northeast of Alutaguse, contains thick Fe- and S-rich quartzites, high-Al garnet-cordierite-sillimanite (± Grt ± Crd ± Sil) gneisses, and Ca-rich and -poor pyroxene-amphibole-biotite gneisses, and has experienced granulite facies metamorphism (Bogdanova et al. 2015; Soesoo et al. 2020; Nirgi and Soesoo 2021).

The Alutaguse zone is characterized by high-temperature amphibolite-facies conditions (Fig. 1a1), with pressures estimated at around 3–5 kbar (Puura et al. 1983). It prominently features metapelites, Al-rich mica gneisses, graphite gneisses, and biotite-plagioclase gneisses, along with some metavolcanic pyroxenic gneiss sequences and felsic/mafic intrusions (Kivisilla et al. 1999; Puura et al. 2004; Kirs et al. 2009; Bogdanova et al. 2015; Soesoo et al. 2020). The metasedimentary Alutaguse zone is considered to be part of the large Kalevian-age (1.9–1.8 Ga) marginal basin that extends to the vicinity of St. Petersburg and Novgorod in Russia, and farther east to Lake Ladoga. However, the ages of deposition and metamorphism of the Alutaguse metasedimentary sequence are still unknown and must be determined before its tectonic setting can be established (All et al. 2004; Bogdanova et al. 2015). Our research will focus on the Estonian Alutaguse section (Fig. 1).

Contrastingly, the Tallinn zone covers mafic amphibolite-facies sequences with amphibole gneisses and magnetite quartzites (Kivisilla et al. 1999). Research by Klein (1986) revealed the average mineral contents of different rocks in the Tallinn and Alutaguse zones, calculated from drill core data. The results showed that rocks with Al-rich garnet make up 25.4% in Tallinn and 90.45% in Alutaguse, while biotite and plagioclase gneisses account for 24.4% and 1%, respectively. Combinations such as Bi-Pl and Bi-Hbl-Pl comprise 50.2% and 6.1%, respectively. The Estonian–Latvian Granulite Belt, situated in Estonia's west and south, consists of charnockitized amphibolites and biotite-feldspar gneisses at 5–6 kbar (All et al. 2004; Soesoo et al. 2006; Bogdanova et al. 2015).

The Estonian Alutaguse region is overlain by a low-altitude landscape, with the highest point reaching up to 166 m (Fig. 1b1), underlain by Precambrian lithologies that extend to depths ranging from 130 m in the north to 450 m in the south (Fig. 1b2). Furthermore, the Alutaguse zone is characterized by low gravity and magnetic field values (Fig. 1b3, 5), yet notable metalliferous anomalies for elements such as Cu, Pb, and Zn have been recognized in the northern part. These anomalies are geographically related to positive residual potential anomalies (Soesoo et al. 2020; Solano-Acosta et al. 2023; Fig. 1b4, 6). Such anomalies are especially prominent in the Uljaste, Assamalla, and Haljala localities, which have been linked to sulfide-graphite gneisses and quartzites (Kivisilla et al. 1999; All et al. 2004; Soesoo et al. 2020; Figs 1a2 and S1).

3. Materials and methods

Thirteen metasedimentary and three metavolcanic rock samples were collected. These were subjected to whole-rock chemical analyses to evaluate their major, trace, and REE compositions and provenance signatures. X-ray fluorescence (XRF, n = 14) and inductively coupled plasma optical emission spectrometry (ICP-OES, n = 2) were used to determine the major elemental composition. Trace and REEs were analyzed via inductively coupled plasma mass spectrometry (ICP-MS). Sample preparation involved powdering fresh samples to a grain size of less than 200 meshes using an agate mill. The powdered samples were dried at 110 °C for over 24 hours to determine major element abundances. At the Tallinn University of Technology laboratory, an XRF analysis was performed on major element concentrations from the Alutaguse samples. The sam-ples were transformed into glass beads using a fusion method that involved a 1:1 mix of lithium

tetra- and metaborate for macroelements in XRF procedures. Every bead consisted of 1 gram of the sample combined with 10 grams of borate, followed by fusion. The loss on ignition (LOI) value was established based on the total weight loss after igniting at 1000 °C for two hours. The XRF measurements were calibrated with the SPECplus software (Malvern Panalytical, Netherlands), with validation ensured through the GeoPT international proficiency tests. At Origin Analytical Limited (UK), the ICP-MS and ICP-OES analyses followed the ISO 9001:2015 standards. ICP-MS and ICP-OES adhered to the GeoPT program calibration, which aims for international rock standard characterization. The trace and major element concentrations were analyzed with the ICP techniques using a SCIEX ELAN 6000 ICP-MS by PerkinElmer (USA).

In the last century, detailed geochemical measurements of the Estonian Precambrian basement lithologies were conducted using traditional silicate analysis techniques, known as wet chemistry, at the laboratory of the Geological Survey of Estonia (EGT), providing valuable information on whole-rock major element geochemistry. All these results were compiled by Kivisilla et al. (1999) into a large dataset, exposing major elemental concentrations (SiO_2, TiO_2, Al_2O_3, Fe_2O_{3tot}, MnO, MgO, CaO, Na_2O, K_2O, P_2O_5, SO_3, LOI; wt%) of the Estonian basement units. Here, we used the major element data from Kivisilla et al. (1999) for the metasedimentary and metavolcanic samples from the Alutaguse zone (n = 229; Table S1). The complete dataset from Kivisilla et al. (1999) is available in the Estonian geoscience literature database, as part of the SARV geological information system (https://kirjandus.geoloogia.info/reference/21247).

The EGT has recently published geochemical trace element data from multiple drill cores in the Uljaste zone (Fig. 1a2). This dataset is presented in the supplementary material and primarily includes trace elements. Major elements, such as silica, and most REEs, except for La and Ce, are notably lacking. We have incorporated these new data into our comprehensive Alutaguse elemental analysis (n = 149; Table S2). The complete Alutaguse trace element dataset is available for download through eMaapõu, an Estonian geological data service managed by institutions such as the EGT, Estonian Land Board, and universities (https://geoloogia.info/analysis?analysisQ=Uljaste&page=1&itemsPerPage=25&method=26).

The complete geochemical dataset with the proper ID, core, coordinates, depth, and references for the analyzed lithological units is available in the supplementary material.

4. Geochemical data and processing

The comprehensive analyses of major, trace, and REEs in sixteen newly examined Alutaguse samples are detailed in Tables 1 and 2, respectively. These new major element data were integrated with the existing dataset from Kivisilla et al. (1999) for an enhanced comparative analysis. Similarly, the newly acquired trace element data were integrated and analyzed alongside the information provided by the Estonian Geological Service, utilizing their lithological sampling

Table 1. Major bulk-rock element data of the 16 novel Alutaguse metasedimentary and metavolcanic samples

		Drill core	Analytic method	ID-code	Lithology	SiO_2	TiO_2	Al_2O_3	Fe_2O_{3tot}	MnO	MgO	CaO	Na_2O	K_2O	P_2O_5	SO_3	LOI	Sum
Metasediments	High-SiO_2	F268	XRF	F2683025	Garnet-bearing mica gneisses ± Crd ± Sil	74.81	0.47	10.96	3.46	0.03	1.64	1.78	1.86	2.39	0.02	0.03	1.32	98.78
		F199	XRF	F1992940	Graphite-bearing mica gneisses ± Grt ± Crd ± Sil	65.64	0.83	16.35	4.03	0.04	2.42	0.20	0.72	6.12	0.06	0.06	2.63	99.10
	Low-SiO_2	F268	XRF	F2682485	Garnet-bearing mica gneisses ± Crd ± Sil	58.50	0.69	17.41	9.67	0.23	3.59	1.52	1.41	5.65	0.02	0.04	1.06	99.80
		F189	XRF	F1893010	Graphite-bearing mica gneisses ± Grt ± Crd ± Sil	57.18	1.16	11.80	11.85	0.10	4.53	2.61	1.42	2.41	0.20	0.12	5.56	98.94
		F189	XRF	F1893089	Graphite-bearing mica gneisses ± Grt ± Crd ± Sil	56.27	0.69	15.83	10.25	0.12	4.74	3.30	1.82	2.15	0.04	0.08	3.49	98.78
		F152	XRF	F1523492	Graphite-bearing mica gneisses ± Grt ± Crd ± Sil	55.25	0.97	15.03	11.49	0.05	4.35	0.46	0.70	6.29	0.02	0.11	4.26	98.99
		F189	XRF	F1893050	Graphite-bearing mica gneisses ± Grt ± Crd ± Sil	52.16	1.21	13.39	12.95	0.11	4.98	2.41	1.37	3.15	0.21	0.25	6.53	98.73
		F255	XRF	F2553994	Graphite- bearing mica gneisses	51.99	0.53	11.49	16.39	0.10	5.52	0.37	0.52	2.02	0.08	0.31	9.97	99.29
		F152	XRF	F1523600	Graphite- bearing mica gneisses	51.89	0.72	12.66	16.97	0.03	3.31	1.32	1.65	4.74	0.04	0.04	5.56	98.93
		F189	ICP-OES	F1893041	Graphite-bearing mica gneisses ± Grt ± Crd ± Sil	51.86	0.90	13.76	13.49	0.10	3.49	2.09	1.37	2.69	0.15	5.75	–	95.64
		F189	XRF	F1893328	Graphite-bearing mica gneisses ± Grt ± Crd ± Sil	46.37	0.80	16.00	15.57	0.29	4.21	3.09	1.91	3.90	0.06	0.15	6.73	99.09
		F268	XRF	F2682450	Graphite-bearing mica gneisses ± Grt ± Crd ± Sil	44.76	2.33	13.86	10.91	0.28	4.11	6.42	0.07	1.98	0.22	1.74	12.55	99.23
		F189	ICP-OES	F1893070	Graphite-bearing mica gneisses ± Grt ± Crd ± Sil	44.57	1.06	14.26	18.44	0.15	5.37	2.47	1.42	2.73	0.14	9.32	–	99.92
Metavolcanics		F189	XRF	F1893458	2-Pyroxene gneisses	45.77	1.05	12.53	13.04	0.23	6.93	9.11	0.22	0.56	0.09	1.87	8.49	99.90
		F268	XRF	F2683260	2-Pyroxene gneisses	52.01	2.25	13.32	11.44	0.18	10.11	2.76	0.91	4.38	0.08	0.11	1.61	99.17
		F255	XRF	F2553248	Pyroxene gneisses	51.45	1.14	14.68	12.71	0.29	7.77	9.84	0.53	0.44	0.10	0.42	0.38	99.74

Table 2. Trace and REE bulk-rock data of the 16 novel Alutaguse metasedimentary and metavolcanic samples (presented in two parts)

		ID code	Be	V	Cr	Co	Ni	Cu	Zn	Ga	Rb	Sc	Sr	Y	Zr	Nb	Mo	Sn	Cs
Metasediments	High-SiO_2	F2683025	1.24	58.48	60.73	105.11	36.68	21.23	90.58	16.41	96.12	7.46	167.90	8.32	151.36	13.04	2.64	0.66	0.66
		F1992940	1.29	122.37	129.65	76.90	30.37	27.51	116.38	21.89	185.82	7.93	112.52	19.61	227.50	15.62	0.33	0.51	3.39
	Low-SiO_2	F2682485	0.98	115.22	117.90	67.64	33.79	8.36	115.84	18.67	156.58	35.14	196.02	82.47	300.37	13.08	0.84	0.35	0.88
		F1893010	2.56	294.94	131.38	83.25	93.88	134.77	406.79	17.79	117.35	13.99	99.83	25.02	167.62	19.44	18.28	0.87	4.57
		F1893089	7.17	239.15	255.66	82.89	72.17	265.58	224.55	20.65	69.48	19.63	128.90	29.50	131.99	8.79	11.57	0.61	3.47
		F1523492	1.83	206.87	138.47	76.83	50.60	401.43	831.34	23.78	214.83	10.87	87.77	4.22	266.42	25.44	3.55	0.56	2.02
		F1893050	2.01	342.43	160.35	70.36	87.50	128.81	572.05	19.89	155.84	17.23	112.01	28.76	181.96	22.64	10.76	1.33	5.87
		F2553994	4.32	214.97	87.86	52.74	36.97	41.48	316.60	17.95	144.32	17.02	25.99	20.48	112.81	10.81	13.04	2.26	10.66
		F1523600	0.93	233.65	123.38	73.87	74.09	578.78	183.68	19.85	175.12	16.25	111.14	15.67	159.98	21.82	8.40	0.44	1.73
		F1893041	3.41	312.29	122.99	72.10	111.05	146.88	438.49	18.79	107.93	15.73	123.22	29.48	155.64	17.27	19.78	1.13	4.32
		F1893328	1.35	245.79	147.55	60.74	104.18	99.65	270.07	19.59	103.19	27.39	144.46	48.90	146.22	10.92	11.99	0.67	1.67
		F2682450	13.48	512.33	87.85	66.16	43.28	54.18	206.71	20.18	44.07	45.94	49.25	33.99	145.31	8.82	1.62	0.47	2.28
		F1893070	3.15	288.55	178.71	62.21	125.11	154.26	235.84	21.46	120.36	33.41	117.05	61.73	156.22	16.00	19.02	0.83	3.94
Metavolcanics		F1893458	1.31	282.53	62.91	53.89	30.56	167.07	377.37	15.42	16.94	39.34	173.58	23.64	64.00	4.94	1.65	0.87	0.89
		F2683260	0.97	436.00	938.45	72.97	134.52	25.94	689.20	26.05	224.00	48.57	82.61	13.97	119.56	29.24	0.83	2.04	7.65
		F2553248	1.15	310.30	92.62	67.76	33.66	54.98	258.79	18.53	15.77	47.19	270.00	29.19	76.18	4.01	2.10	0.59	0.94

		ID code	Ba	La	Ce	Pr	Nd	Sm	Eu	Gd	Tb	Dy	Ho	Er	Tm	Yb	Lu	Hf	Ta	Pb	Th	U
Metasediments	High-SiO_2	F2683025	832.70	79.87	145.73	15.90	52.80	6.39	1.30	5.11	0.49	1.69	0.32	0.92	0.13	0.80	0.12	4.42	0.57	21.48	23.50	0.67
		F1992940	844.42	42.66	79.75	9.85	35.11	6.06	1.26	5.16	0.71	3.58	0.73	2.09	0.31	2.13	0.32	6.53	1.13	12.83	16.32	2.26
	Low-SiO_2	F2682485	1707.24	27.63	46.20	4.97	17.07	3.28	1.74	5.34	1.33	10.66	2.94	9.59	1.61	11.85	1.89	8.58	0.60	32.88	5.44	0.70
		F1893010	471.79	38.25	72.91	9.32	34.76	6.67	1.49	6.26	0.91	4.63	0.93	2.42	0.35	2.29	0.35	4.54	1.74	2.78	10.61	7.27
		F1893089	382.53	48.08	92.49	11.68	43.52	7.93	1.68	7.29	0.98	5.09	1.15	3.27	0.51	3.70	0.63	3.89	0.84	7.40	17.32	3.52
		F1523492	826.77	23.38	41.58	4.66	16.51	2.46	1.17	2.12	0.22	0.75	0.14	0.37	0.06	0.39	0.07	7.74	1.37	215.11	5.30	0.69
		F1893050	529.25	46.13	88.01	11.28	43.03	8.12	1.82	7.51	1.07	5.43	1.10	2.85	0.39	2.57	0.39	5.09	1.74	10.77	12.66	6.83
		F2553994	283.49	24.91	51.65	6.13	22.28	4.54	0.66	4.38	0.70	3.86	0.83	2.31	0.36	2.56	0.42	3.38	0.98	9.10	11.41	6.76
		F1523600	551.97	57.21	106.92	12.80	45.82	7.44	1.27	6.40	0.78	3.35	0.60	1.49	0.18	1.08	0.17	4.77	1.32	5.02	22.51	2.87
		F1893041	460.37	42.49	79.41	10.16	37.35	7.04	1.52	6.62	0.97	5.17	1.11	2.92	0.41	2.72	0.43	4.31	1.48	9.91	13.44	8.79
		F1893328	1032.26	41.87	79.44	9.53	34.50	6.03	1.80	6.14	1.09	7.34	1.79	5.33	0.83	5.68	0.87	4.22	0.86	6.25	12.55	2.56
		F2682450	577.20	5.33	13.76	2.14	10.51	3.11	1.07	4.01	0.82	5.55	1.33	3.67	0.56	3.96	0.60	4.37	0.78	123.90	0.60	1.01
		F1893070	439.50	44.48	85.40	10.67	40.01	7.81	2.02	7.69	1.35	9.17	2.33	6.83	1.01	7.12	1.11	4.62	1.23	5.20	14.69	3.60
Metavolcanics		F1893458	369.12	7.32	16.19	2.29	9.81	2.81	1.10	3.31	0.64	3.92	0.90	2.54	0.39	2.49	0.38	1.80	0.58	6.66	1.20	0.95
		F2683260	630.36	5.16	11.21	1.55	6.55	1.69	0.92	1.99	0.34	2.10	0.48	1.34	0.22	1.50	0.24	3.73	2.00	7.09	0.43	1.09
		F2553248	309.62	10.68	23.88	3.30	14.60	3.72	1.39	4.26	0.80	4.73	1.08	2.98	0.44	2.97	0.42	2.24	0.45	7.03	0.66	0.46

classification system, which was aligned with the drilling core descriptions from the same source, accessible at https://gis.egt.ee/portal/apps/dashboards/99f758ac4ef548f686b831adb3199378. Consistency in classifying all analyzed units was ensured by adopting the system outlined by Kivisilla et al. (1999). Table S1 presents the average concentrations of major elements (wt%) found in Alutaguse metasediments, while Table S2 details the average concentrations of trace and REEs (ppm). Bulk-rock major element concentrations, excluding LOI, were normalized to 100% for the samples. Non-normalized LOI values were considered separately when necessary.

The Alutaguse samples were categorized based on their silica concentrations (Verma and Armstrong-Altrin 2013; Chen et al. 2014), distinguishing between high-SiO_2 (>63 wt%) and low-SiO_2 (<63 wt%; Fig. S2). This classification, following Verma and Armstrong-Altrin (2013), helped identify the discriminant functions of distinct tectonic settings and provenance characteristics.

The high-SiO_2 group includes lithologies such as biotite gneisses, garnet-bearing mica gneisses ± Crd ± Sil, cordierite-bearing mica gneisses ± Grt ± Sil, and graphite-bearing mica gneisses ± Grt ± Crd ± Sil. Conversely, the low-SiO_2 group comprises lithologies with similar mineralogical compositions but with silica values (χSiO_2) <63 wt%, including biotite gneisses ± Grt ± Crd ± Sil, garnet-bearing mica gneisses ± Crd ± Sil, and graphite-bearing mica gneisses ± Grt ± Crd ± Sil. Due to the absence of major element data from the Estonian Geological Service, these units were theoretically classified based on their lithological classification and the preference for high or low silica content for each lithology (Table S2). Novel Alutaguse samples were also classified based on their silica content (Tables 1 and 2).

Metavolcanic rocks in the region, such as amphibolites and pyroxene gneisses, have not been further subclassified and are broadly categorized based on their amphibole and pyroxene content (Table S2). For a more detailed explanation of the lithological classification used in this study, please refer to the supplementary material.

5. Results

Metasedimentary sample values from the Alutaguse region were compared with established geochemical references, including the upper continental crust (UCC; Rudnick and Gao 2003) and post-Archean Australian shale (PAAS; Taylor and McLennan 1985; McLennan 2001). Metavolcanic samples were compared with the primitive mantle (PM) reference (Sun and McDonough 1989).

5.1. Geochemistry of major elements

Figure 2a illustrates the Al_2O_3 Harker binary plots (Harker 1909) for Alutaguse metasedimentary rocks, showing high-SiO_2 samples aligning with UCC, while low-SiO_2 samples resemble PAAS. TiO_2, MgO, and CaO concentrations are higher in low-SiO_2 metasediments. Additionally, the MgO Harker metavolcanic plots reveal higher Ti and Fe concentrations compared to the metasediments units (Fig. 2b), with a positive correlation between Ti, Fe, and Ca contents, especially in the 2-pyroxene gneiss samples.

According to geochemical lithological classifications, high-SiO_2 samples predominantly fall within the litharenite domain, while low-SiO_2 samples align with graywacke and shale zones, as indicated by Herron (1988; Fig. S3a) and Pettijohn et al. (1987; Fig. S3b) plots.

High-SiO_2 metasediments had an average SiO_2 content of 69.31%, ranging from 63.25% to 80.20%, suggesting minimal chemical alteration and a more uniform geochemical profile (Chen et al. 2014). This group (Fig. 3a) also displayed narrower ranges of oxides, such as Al_2O_3 (10.21% to 19.03%), Fe_2O_3 (0.00% to 14.42%), MnO (0.01% to 0.47%), and MgO (0.52% to 5.10%). The SO_3 content (0.00% to 4.61%) was insignificant. Conversely, low-SiO_2 samples (Fig. 3b) exhibited a moderate average SiO_2 content of 54.81%, with a broader range from 29.49% to 62.80%, suggesting more substantial chemical alteration and source variability, mostly mafic. This group showed broader oxide ranges, such as Al_2O_3 (7.59% to 28.07%) and Fe_2O_3 (5.56% to 32.59%). Other oxides, including MgO (0.67% to 8.56%) and MnO (0.01% to 1.01%), also presented more extensive ranges. SO_3 content was significant (0.00% to 23.09%), particularly over graphite mica gneisses (Table 1).

Using the total alkali-silica (TAS) classification by Le Bas et al. (1986), metavolcanic samples show low Na_2O, K_2O, and SiO_2 concentrations, aligning with the subalkaline series, which span from basaltic to andesite zones. Metavolcanic samples predominantly align with the ortho-amphibolite domain (Fig. S3c). A pronounced tholeiitic trend is observed on the AFM diagram (Fig. S3d), with most samples distributed across the high-Fe tholeiitic zone (HFT) in the Jensen (1976) plot (Fig. S3d). High Mg# values are observed in the Alutaguse metavolcanic samples, ranging from 34.87 to 68.40, with an average of 51.83, resembling the tholeiitic basalt magma fractionation trend (Casey et al. 2007).

Figure 3c presents major element data for metavolcanic rocks displayed on spider diagrams, normalized to the PM as specified by McDonough and Frey (1989). The data illustrate broader ranges in Na_2O and K_2O concentrations, particularly within the 2-pyroxene gneiss lithologies. Among the major oxides, MgO shows a depletion relative to the PM standard, while others, such as TiO_2 and K_2O, appear elevated.

Metavolcanic samples present an average SiO_2 content of 52.60%, ranging from 38.96% to 62.67%. The TiO_2, Al_2O_3, and Fe_2O_3 concentrations in the metavolcanic rocks are notably higher compared to the high-SiO_2 group, with averages of 1.20% (0.57% to 2.90%), 13.46% (8.99% to 17.54%), and 12.65% (7.14% to 18.65%), respectively. These values are similar to those found in the low-SiO_2 samples, emphasizing the enriched and diverse mineral content of the metavolcanic rocks. Notably, the rocks exhibit higher concentrations of MgO and CaO, with averages of 7.11% (3.60% to 13.13%) and 9.10% (2.83% to 13.16%), respectively, which exceed the values observed in both metasedimentary groups. Minor oxides, Na_2O and K_2O show averages of 1.15% and 1.16%

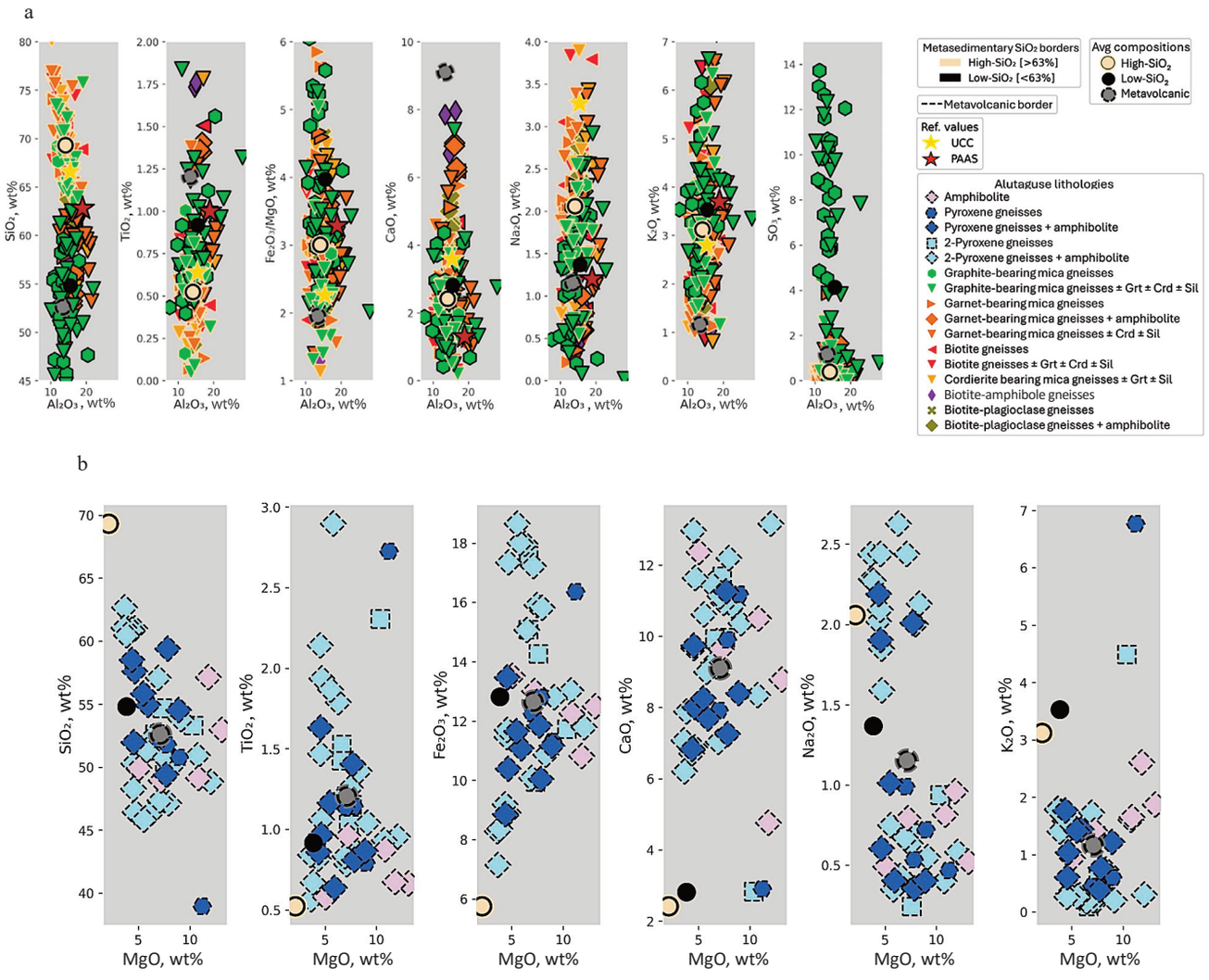

Fig. 2. Harker binary plots of Alutaguse samples: **a** – metasedimentary major oxides vs. Al_2O_3, with metasedimentary samples compared against upper continental crust (UCC) and post-Archean Australian shale (PAAS) references; **b** – metavolcanic major oxides vs. MgO, showing markers per lithology with borders representing sample groups: high-SiO_2 (wheat), low-SiO2 (black), and metavolcanics (dashed gray). Average values for each group are plotted on both graphs.

(0.24% to 2.63% and 0.10% to 6.77%, respectively), while SO_3 averages at 1.17% (maximum value 7.15%).

5.2. Geochemistry of trace and rare earth elements

Transition elements, such as Cr, Ni, Sc, and V, are commonly found in mafic rocks and resist dispersion from secondary processes (Chen et al. 2014). High-SiO_2 units (Fig. 3d) have average concentrations of 85.21 ppm for Cr, 123.96 ppm for V, 50.66 ppm for Ni, and 14.20 ppm for Sc, with ranges of 16.00–203.00, 8.00–277.00, 2.50–195.00, and 3.70–36.00 ppm, respectively. On the other hand, low-SiO_2 rocks show slightly higher average values, with 101.42 ppm for Cr, 208.05 ppm for V, 120.14 ppm for Ni, and 15.6 ppm for Sc, alongside broader ranges of 14.00–432.00, 12.00–529.00, 8.30–385.00, and 0.60–55.40 ppm, respectively. The low-SiO_2 metasediments, in particular, exhibit a significant valley in Sc concentrations, especially evident in samples from graphite-bearing mica gneisses (Fig. 3e).

Metavolcanic rocks, however, exhibit the greatest variability and the highest average concentrations, especially for Cr and Sc. Cr ranges from 13.00 to 938.00 ppm, with an average of 149.75 ppm; V ranges from 29.00 to 471.00 ppm, averaging 235.49 ppm; Ni ranges from 16.80 to 210.00 ppm, with an average of 88.44 ppm, and Sc ranges from 1.00 to 52.80 ppm, averaging 26.80 ppm. Metavolcanic rocks have higher Cr and V levels than high-SiO_2 and low-SiO_2 metasedimentary groups. Spider diagrams of PM-normalized trace element data for the Alutaguse metavolcanic rocks suggest significant depletion of Cr and Ni in the examined samples, alongside Sc and V averages that are normalized against the PM (Fig. 3f).

Regarding the large-ion lithophile elements (LILE), such as Ba, Rb, Pb, and Sr, the high-SiO_2 samples show average Ba, Rb, Pb, and Sr concentrations of 804.89, 110.54, 24.44, and 203.98 ppm, respectively. Their ranges extend from 190.00 to 1570.00, 59.40 to 202.00, 7.50 to 65.50, and 35.50 to 462.00 ppm, respectively. The low-SiO_2 group shows a lower average Ba concentration at 520.58 ppm but a higher Pb concentration at 101.59 ppm. The average Rb and Sr concentrations are similar to those of the high-SiO_2 group, at 110.63 ppm and 132.80 ppm, respectively. The ranges for these elements in the low-SiO_2 rocks are wider, especially

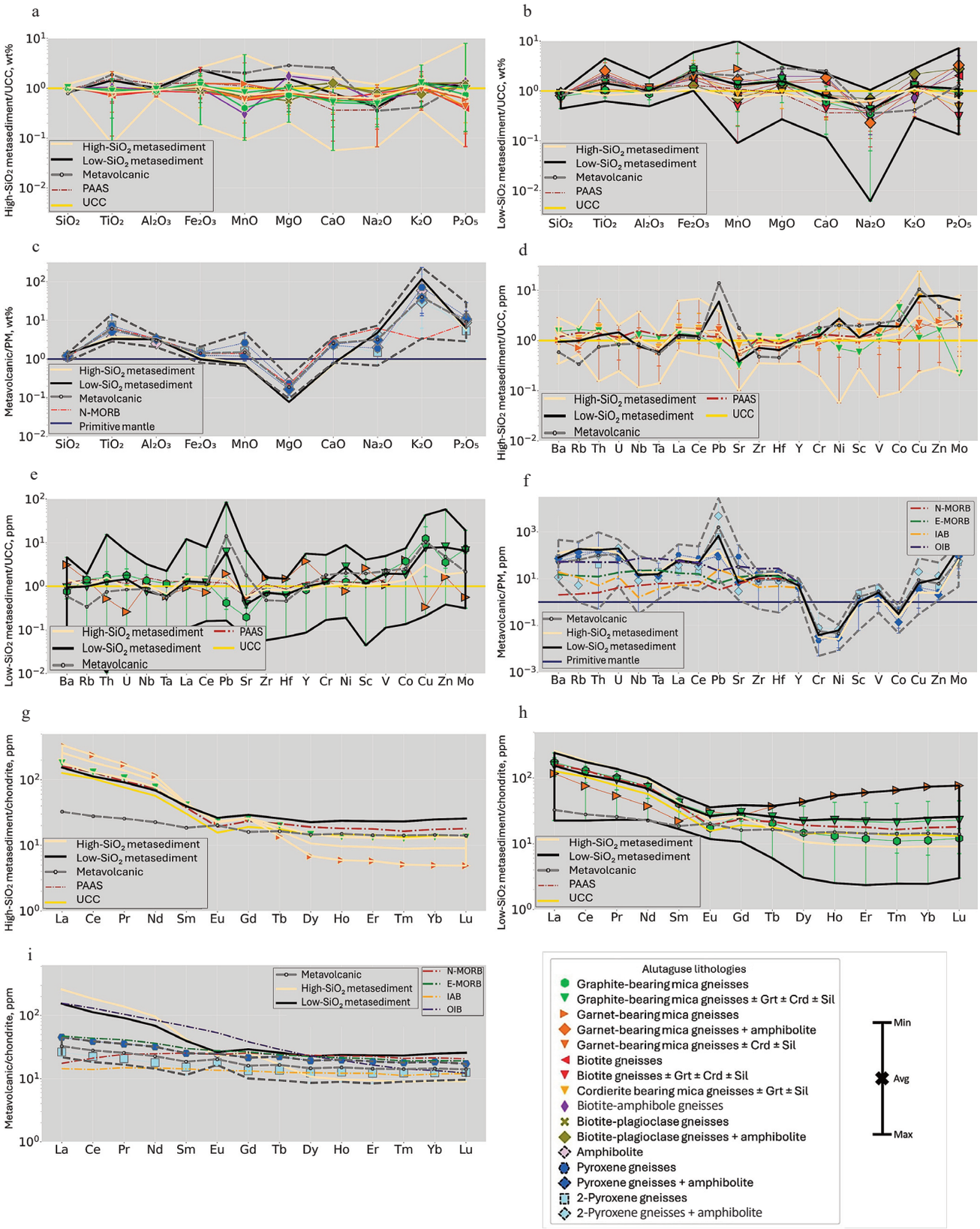

Fig. 3. Normalized spider plots of Alutaguse samples: **a**, **b** – upper continental crust (UCC)-normalized major element data for high-SiO_2 and low-SiO_2 metasediments (Rudnick and Gao 2003); **c** – primitive mantle (PM)-normalized major element data for metavolcanic samples (Sun and McDonough 1989); **d**, **e** – UCC-normalized trace element data for high-SiO_2 and low-SiO_2 metasediments; **f** – PM-normalized major element data for metavolcanic samples; chondrite-normalized (Sun and McDonough 1989) REE data for **g** – high-SiO_2 metasediments, **h** – low-SiO_2 metasediments, and **i** – metavolcanic samples. Abbreviations: N-MORB – normal mid-ocean ridge basalt, E-MORB – enriched mid-ocean ridge basalt, IAB – island arc basalt, OIB – oceanic island basalt.

for Ba (30.00–2540.00 ppm) and Sr (24.00–2230.00 ppm). Pb concentrations range up to 1430.00 ppm, particularly in the graphite gneiss samples.

Metavolcanic rocks exhibit the most significant variability in composition, particularly for trace elements, such as Pb and Sr. Compared to both the high-SiO_2 and low-SiO_2 groups, they display wider ranges across all analyzed LILEs. On average, the Ba, Rb, Pb, and Sr concentrations are 323.10, 37.93, 238.24, and 623.45 ppm, respectively. The ranges for these elements are remarkably wide, from 50.00 to 3030.00, 0.60 to 224.00, 1.40 to 4030.00, and 24.60 to 5530.00 ppm, respectively.

High field strength elements (HFSE), such as Nb, Ta, Zr, Hf, Th, and U, exhibit incompatibility during magma crystallization and anatectic processes. This leads to their preferential concentration in felsic rocks (Feng and Kerrich 1990; Han et al. 2019). In high-SiO_2 samples, the average concentrations of Nb, Ta, Zr, Hf, Th, and U are 12.69, 0.67, 159.74, 4.66, 16.79, and 2.45 ppm, respectively. The ranges for these elements are fairly broad, particularly for Nb (1.40–45.30 ppm) and Zr (67.20–227.50 ppm). Low-SiO_2 units show slightly lower average concentrations of Nb (9.20 ppm) and Ta (0.59 ppm) but similar levels of Zr (135.61 ppm) and Hf (3.74 ppm), with lower averages for Th (13.21 ppm) and U (3.93 ppm). The ranges for these elements are even broader than those of the high-SiO_2 group, with Zr ranging from 11.00 to 300.37 ppm, and Th and U exhibiting considerable variability (Th: 0.11–160.00 ppm; U: 0.30–17.20 ppm).

Alutaguse metavolcanic rocks display the widest range but intermediate average values for HFSEs. The average concentrations are 10.23 ppm for Nb, 0.55 ppm for Ta, and 90.75 ppm for Zr. The ranges are 0.20–62.20, 0.05–2.00, and 5.30–202.00 ppm, respectively. Hf concentrations range from 0.10 to 5.90 ppm, Th concentrations from 0.04 to 76.50 ppm, and U concentrations from 0.10 to 9.50 ppm, with respective averages of 2.66, 7.82, and 2.26 ppm. Metavolcanic rocks encompass a broader range of trace element concentrations and generally align more closely with the low-SiO_2 group in terms of average values, except for Ta and U, where they show lower averages (Table S2).

The REE analysis of the 16 new samples from Alutaguse (Table 2) reveals that the high-SiO_2 group (Fig. 3g) exhibits a higher total REE (ΣREE) average of 250.65 ppm, predominantly consisting of light REEs (LREE; La–Gd) at 243.48 ppm and comparatively lower heavy REEs (HREE; Tb–Lu) at 7.18 ppm. ΣREE ranges from 189.73 to 311.58 ppm, LREEs range from 179.85 to 307.10 ppm, and HREEs from 4.47 to 9.88 ppm. In con-trast, the low-SiO_2 group (Fig. 3h) shows a lower ΣREE average of 174.94 ppm, but higher HREEs at 16.70 ppm, ranging from 2.00 to 39.87 ppm, and LREEs averaging 158.24 ppm, with a range of 39.93 to 237.86 ppm. Chondrite-normalized REE patterns for both high-SiO_2 (Fig. 3g) and low-SiO_2 samples (Fig. 3h) align closely with UCC and PAAS references, showing LREE enrichment, flat HREE profiles, no Ce anomalies, and similar negative Eu anomalies, whereas Alutaguse metavolcanic samples (Fig. 3i) exhibit null to slightly positive Eu anomalies (Table S2).

Metavolcanic samples exhibit the lowest REE concentrations, with an average ΣREE content of 54.88 ppm (35.29–75.26 ppm), LREEs averaging 44.58 ppm (29.07–61.84 ppm), and HREEs averaging 10.30 ppm (6.22–13.43 ppm). Overall, this pattern suggests that, although high-SiO_2 and low-SiO_2 groups have higher concentrations of REEs, particularly LREEs, the metavolcanic rocks, despite their lower ΣREE content, show a relatively higher proportion of HREEs (Fig. 3i).

6. Discussion

Multiple geological factors influence the geochemical composition of basin lithological units, including chemical weathering and alteration, as explored in both metasedimentary and metavolcanic contexts (Taylor and McLennan 1985; Gao and Wedepohl 1995; Cullers et al. 1997; Gao et al. 1999; Large et al. 2001; Sifeta et al. 2005; Karakaş and Güçtekin 2021). For metasediments, key determinants include: 1) transport and sedimentation sorting (McLennan et al. 1993; Cullers 1994), 2) diagenesis or metamorphism during burial (Fedo et al. 1995, 1996), and 3) sediment origin and deposition environment (Bhatia and Crook 1986; Roser and Korsch 1986). Thus, evaluating the impact of these factors on the chemical profiles of the Alutaguse samples is crucial before drawing petrogenetic conclusions. Subsequent sections delve into the geochemistry of both metasediments and metavolcanics, shedding light on their tectonic and compositional nuances (Bhatia and Crook 1986; Roser and Korsch 1986; McLennan et al. 1993; Cullers 1994; Fedo et al. 1995, 1996; Large et al. 2001; Sifeta et al. 2005; Bailie et al. 2011; Jian et al. 2013; Faisal et al. 2020; de Carvalho Mendes et al. 2021).

6.1. Weathering and alteration indices

During weathering, elements such as Na, K, and LILEs are depleted, while Al_2O_3, TiO_2, REEs, and HFSEs become enriched. Despite this, HFSEs and REEs exhibit limited changes due to their inherent immobility during weathering (McLennan 1989, 1993; Cullers et al. 1997). To determine the mineralogical and chemical changes that occur in the analyzed metasediments as a result of alteration, various chemical alteration indices are used, such as the chemical index of alteration (CIA; Nesbitt and Young 1982), the plagioclase index of alteration (PIA; Fedo et al. 1995), the chemical index of weathering (CIW; Harnois 1988), and the index of compositional variation (ICV; Cox et al. 1995). For metavolcanic samples, indices such as the Hashimoto alteration index (AI; Ishikawa et al. 1976), the chlorite-carbonate-pyrite index (CCPI; Large et al. 2001), the Parker weathering index (WIP; Parker 1970), and the sericitization index (SI; MacLean and Hoy 1991; Karakaş and Güçtekin 2021) were utilized.

High-SiO_2 metasediments in Alutaguse display CIA values ranging from 47.13 to 75.85, PIA values from 45.60 to 90.67, and CIW values between 55.05 and 94.43, suggesting moderate to intense weathering comparable to UCC averages. Conversely, low-SiO_2 metasediments show more intense weathering, with CIA values ranging from 52.03 to 88.38, PIA values from 53.52 to 99.73, and CIW values nearing

PAAS levels, between 60.99 and 99.76. ICV values reflect sediment maturity, with high-SiO_2 averaging 1.50 and low-SiO_2 averaging higher at 2.06. The Th/U ratio further underscores variations in weathering intensity between these groups, with high-SiO_2 averaging 8.68 and low-SiO_2 4.33.

Metavolcanic samples exhibit hydrothermal alteration influence, demonstrated by relatively high alteration indices and analyses indicating metasomatic changes. These changes are characterized by shifts in mineral compositions and increased alteration intensity, particularly in the basalt/andesite zones of alteration box plots, suggesting profound hydrothermal influences.

The supplementary data further explore the weathering conditions of the analyzed metasedimentary and metavolcanic samples (Fig. S4).

6.2. Metasedimentary rocks

The Alutaguse metasedimentary samples, with a mid-weathered composite index (CIA <80) and chemical immaturity (ICV >1 and SiO_2/Al_2O_3 <6; Table S1), provide reliable data for provenance and tectonic analysis (El-Bialy 2013; Han et al. 2019). Their low LOI averages, below 4% (Table S1), indicate minimal secondary alterations (Han et al. 2019). However, the high LOI values in graphite-bearing mica gneisses warrant cautious interpretation.

6.2.1. Provenance

Al_2O_3/TiO_2 ratios (Fig. S5a), commonly used in rock origin studies, reflect the source rock compositions in sandstones and mudstones. This ratio is consistent between silts, shales, and their sources, as Ti predominantly exists in clay minerals or as ilmenite inclusions, making it a reliable marker for igneous source rocks. Ratios of 3–16, 8–21, and 21–70 indicate mafic, intermediate, and felsic sources, respectively (Hayashi et al. 1997). The Alutaguse high-SiO_2 group averages a ratio of 35.18 (9.90–270.40), while the low-SiO_2 group averages 19.66 (5.17–34.16). Low-SiO_2 metasediments seem to present mafic to intermediate sources closer to PAAS (18.9), contrary to high-SiO_2 samples with higher affinity within UCC (24.06), suggesting felsic sources.

Utilizing the discriminant plot by Roser and Korsch (1988; Fig. 4a), high-SiO_2 metasediments from Alutaguse exhibit a transition from intermediate to felsic origins, whereas low-SiO_2 samples vary from mafic to intermediate, with graphite-bearing mica gneisses predominantly positioned in the mafic zone. The mobility of lithophile elements K and Rb during diagenesis and low-grade metamorphism aids in tracing igneous sources, as demonstrated in the K_2O vs. Rb plots (Fig. S5b), indicating felsic to intermediate origins for these metasediments.

The TiO_2–Ni plot (Fig. 4b) reveals that high-SiO_2 samples predominantly indicate felsic origins, whereas low-SiO_2 samples suggest sedimentary trends from mafic sources. In contrast, transition elements, such as Cr, Sc, Ni, Co, and V, which are typically concentrated in mafic minerals, including pyroxene and olivine, are found to enrich sedimentary rocks derived from mafic igneous sources (Cullers et al. 1997; El-Bialy 2013; Chen et al. 2014). During magma differentiation, felsic rocks maintain higher concentrations of HFSEs, such as Zr, Hf, Th, and U, displaying stability against diagenetic and metamorphic alterations. This stability makes them effective provenance indicators (Feng and Kerrich 1990; Armstrong-Altrin et al. 2004). Table S2 shows that low-SiO_2 samples are characterized by lower HFSE levels, suggesting a mafic source, whereas high-SiO_2 samples exhibit higher HFSE concentrations, likely obscured by quartz dilution (Chen et al. 2014), reflecting a significant felsic source influence (Table S2).

Elemental ratios, such as La/Sc and Th/Sc, effectively distinguish between mafic and felsic sources (Table 3). High-SiO_2 metasediments align with felsic source signatures, while low-SiO_2 samples show elevated ratios indicative of an intermediate source. Th and Zr, predominantly found in felsic rocks due to their incompatibility in igneous processes, contrast with Sc, which is present in early-forming mafic minerals, such as olivine and pyroxene (McLennan and Taylor 1991). The ratios of Th/Sc and Zr/Sc for Alutaguse metasediments (Fig. S5c) generally trace the igneous differentiation path from andesite to granite, with low-SiO_2 samples showing lower ratios indicative of basaltic influences – a trend supported by the binary plots of La/Th vs. Hf (Fig. S5d) and La/Sc vs. Co/Th (Fig. 4c).

REEs, with their low partition coefficients between water and rock, readily transfer from source rocks to clasts, maintaining stability through weathering, transport, diagenesis, and medium-grade metamorphism, which makes them robust provenance indicators (Chaudhuri and Cullers 1979; McLennan 1989; Gao and Wedepohl 1995; Cullers et al. 1997). While mafic igneous rocks typically exhibit low REE concentrations without significant negative Eu anomalies, felsic rocks display higher REE concentrations with pronounced negative Eu anomalies (Cullers et al. 1997). Chondrite-normalized REE patterns for Alutaguse metasediments (Fig. 3g, h) show substantial LREE to HREE fractionation, indicative of predominantly intermediate to felsic source contributions (Chen et al. 2014). These patterns, featuring marked negative Eu anomalies, suggest extensive feldspar fractionation within their parent rocks (Han et al. 2019) and are consistent with a composition rich in quartz and chlorite (McLennan 1993). The negative Eu anomaly typically aligns with differentiated silicic sources, similar to granitic origins (Condie 1993; McLennan 1993; Gao and Wedepohl 1995; Gu et al. 2002). Eu/Eu* values, indicating differentiation, are slightly higher in high-SiO_2 samples, averaging 0.52 (ranging from 0.27 to 0.76), compared to low-SiO_2 samples at 0.43 (ranging from 0.22 to 0.77), as shown in Table S2.

6.2.2. Sorting, recycling and maturation

Sorting during sedimentary transport significantly influences the mineralogical and chemical characteristics of sediments. Textural maturity, evaluated through grain sizes, morphologies, and mineralogical and geochemical profiles, offers insights into the sorting process (McLennan et al. 1993). Lower SiO_2/Al_2O_3 ratios are indicative of minimal sedimentary sorting (Taylor and McLennan 1985; Rudnick and Gao 2003; Chen et al. 2014). High-SiO_2 specimens exhibit

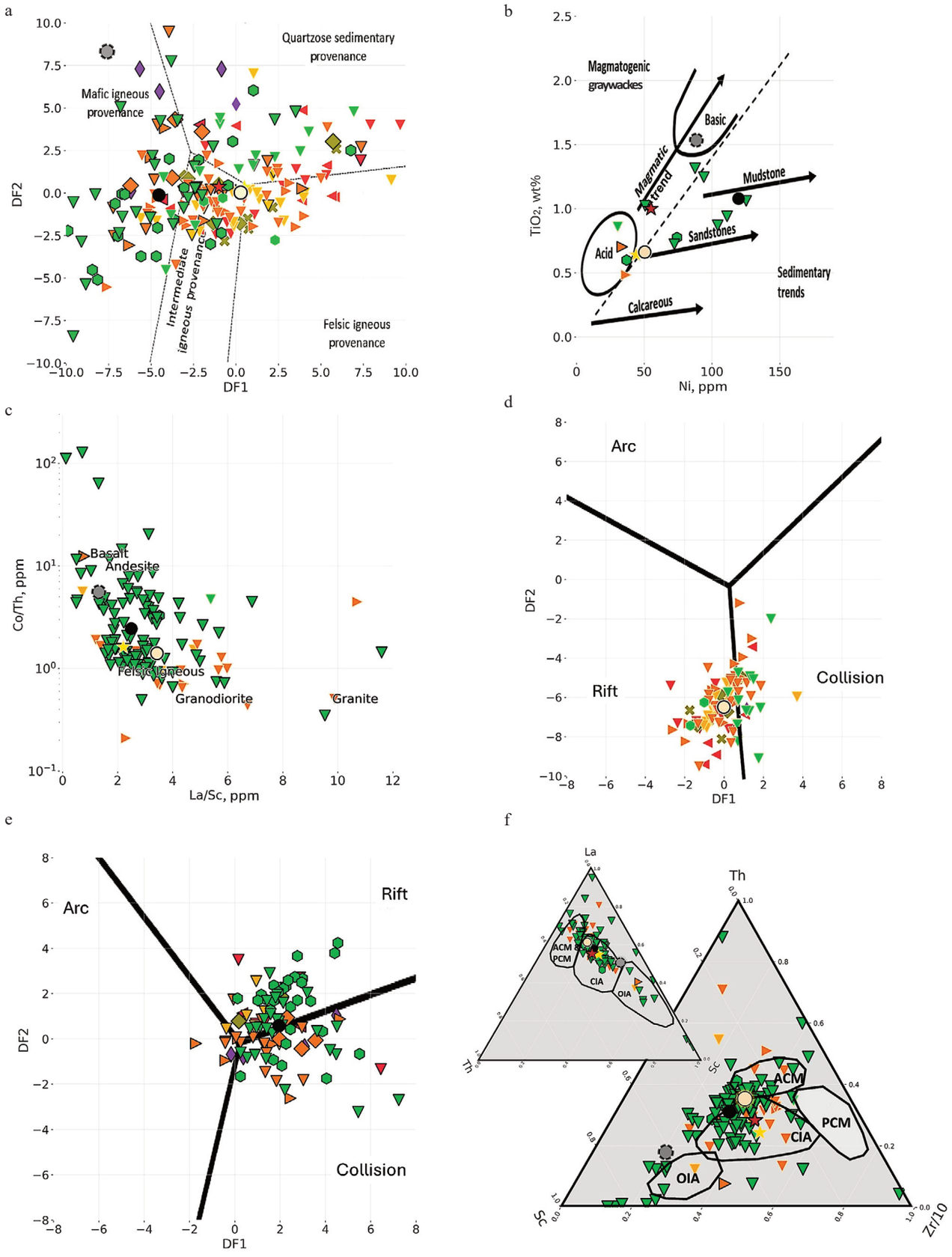

Fig. 4. Source and tectonic setting plots of Alutaguse metasedimentary samples: **a** – discriminant function plot of provenance signatures using major elements, with the accompanying equations (after Roser and Korsch 1988): DF1 = 30.638 TiO_2/Al_2O_3 – 12.541 Fe_2O_3/Al_2O_3 + 7.329 MgO/Al_2O_3 +12.031 Na_2O/Al_2O_3 + 35.402 K_2O/Al_2O_3 – 6.382 vs. DF2 = 36.500 TiO_2/Al_2O_3 – 10.879 Fe_2O_3/Al_2O_3 + 30.875 MgO/Al_2O_3 – 5.404 Na_2O/Al_2O_3 + 11.112 K_2O/Al_2O_3 – 3.89; **b** – TiO_2 vs. Ni plot (after Floyd et al. 1989); **c** – Co/Th vs. La/Sc plot (after Gu et al. 2002); **d**, **e** – tectonic classification of high-SiO_2 and low-SiO_2 metasediments (see Verma and Armstrong-Altrin 2013 for further details on DF1 and DF2 formulas for both groups); **f** – ternary plots of La–Th–Sc (inset) and Th–Sc–Zr/10 (back) (after Bhatia and Crook 1986). Abbreviations: ACM – active continental margin, PCM – passive continental margin, CIA – continental island arc, OIA – oceanic island arc. Sample marker legend as in Figure 2a.

Table 3. Range of elemental ratios for the Alutaguse metasedimentary units compared to the ratios of the upper continental crust (after Rudnick and Gao 2003) and sediments derived from felsic and mafic rocks (after Armstrong-Altrin et al. 2004). Values for Alutaguse are organized as "min–max; avg". High-SiO_2 graphite-bearing mica gneisses ± Grt ± Crd ± Sil lithology represent only one sample (Table S2)

Sample type		La/Sc	La/Co	Th/Sc	Th/Co	Cr/Th
Range of sediments from felsic sources		2.50–16.3	1.80–13.8	0.84–20.05	0.67–19.4	4.00–15.00
Range of sediments from mafic sources		0.43–0.86	0.14–0.38	0.05–0.22	0.04–1.40	25.00–500.00
UCC		2.20	1.79	0.77	0.61	7.53
PAAS		2.39		0.91		7.53
High-SiO_2	Garnet-bearing mica gneisses ± Crd ± Sil	1.20–9.87; 4.28	1.55–13.81; 4.11	0.41–3.74; 1.33	0.53–2.29; 1.10	1.59–16.99; 6.86
	Garnet-bearing mica gneisses	2.03–10.71; 4.86	0.76–10.98; 4.48	0.69–3.15; 1.56	0.22–4.78; 1.75	2.58–8.35; 4.86
	Cordierite-bearing mica gneisses ± Grt ± Sil	0.72–4.77; 3.12	0.58–3.54; 2.44	0.22–1.95; 1.09	0.18–1.09; 0.81	1.76–6.67; 5.28
	Graphite-bearing mica gneisses ± Grt ± Crd ± Sil	5.38	0.55	2.06	0.21	7.94
	Total	**0.72–10.71; 4.19**	**0.55–13.81; 3.71**	**0.22–3.74; 1.35**	**0.18–4.78; 1.11**	**1.59–16.99; 6.29**
Low-SiO_2	Graphite-bearing mica gneisses ± Grt ± Crd ± Sil	0.07–77.87; 4.36	0.03–21.75; 2.02	0.00–33.25; 1.43	0.00–9.64; 0.67	0.30–945.45; 32.18
	Graphite-bearing mica gneisses	1.46–3.52; 2.49	0.47–0.77; 0.62	0.67–1.39; 1.03	0.22–0.30; 0.26	5.48–7.70; 6.59
	Garnet-bearing mica gneisses	0.79	0.41	0.15	0.08	21.69
	Total	**0.07–77.87; 4.29**	**0.03–21.75; 1.98**	**0.00–33.25; 1.41**	**0.00–9.64; 0.65**	**0.30–945.45; 31.60**

an average SiO_2/Al_2O_3 ratio of 5.02 wt%, suggesting greater sorting, compared to 3.65 wt% in their low-SiO_2 counterparts.

The analyzed metasediments display K_2O/Na_2O ratios above 1 wt%, indicating chemical immaturity (El-Bialy 2013), a feature more pronounced in low-SiO_2 samples, showing the highest values (Fig. S5e). Conversely, high-SiO_2 samples exhibit greater maturity, as indicated by higher Al_2O_3/TiO_2 ranges (Hayashi et al. 1997; Fig. S5a).

Provenance discrimination plots by Roser and Korsch (1988) reveal that high-SiO_2 samples fall within the quartzose sedimentary provenance field, suggesting mature, recycled sediments with polycyclic quartzose detritus (Fig. 4a). In contrast, low-SiO_2 samples are derived from primary mafic-magmatic sources. Transport and recycling processes often result in higher CIW values. Sediments from extensive provenance areas display higher CIW/CIA ratios, indicative of longer transport distances and suggesting broader provenance and considerable travel before deposition (Gao et al. 1999; El-Bialy 2013). For the Alutaguse samples, high-SiO_2 specimens have an average CIW/CIA value of 1.17 mol, whereas low-SiO_2 samples average 1.20 mol, with all samples exhibiting CIW/CIA ratios greater than 1 mol, suggesting a long-distance provenance.

Sedimentary materials can be categorized by maturity and recycling into psammitic and pelitic types. Psammitic sediments are generally closer to their source, as indicated by lower maturity and coarser grains. In contrast, pelitic sediments, characterized by finer grains, suggest higher maturity due to extended transport and erosion. Using the 100 × TiO_2/Zr ratio (Garcia et al. 1994), values below 0.33 wt%/ppm are typically psammitic, whereas those above 0.33 wt%/ppm are pelitic. The SiO_2/Al_2O_3 ratio at 4.35 wt% is considered the threshold between these categories (Garcia et al. 1994; El-Bialy 2013). For the high-SiO_2 samples, the 100 × TiO_2/Zr ratio averages 0.35 wt%/ppm, with a SiO_2/Al_2O_3 average of 5.02 wt%, and ranges from 0.32 to 0.38 wt% and 3.49 to 7.80 wt%, respectively, clearly classifying them as psammitic. Conversely, low-SiO_2 samples display more varied characteristics, with averages of 0.67 wt%/ppm for 100 × TiO_2/Zr and 3.65 wt% for SiO_2/Al_2O_3, and ranges from 0.23 to 1.85 wt%/ppm and 1.54 to 5.16 wt%, respectively. These results indicate a mix of pelitic to psammitic properties, depending on the specific metrics considered, suggesting different levels of transport and sedimentary recycling.

Trace elements Zr, Th, and Sc are essential in assessing clastic rock provenance and recycling. The Th/Sc and Zr/Sc ratios, which indicate chemical differentiation and sediment recycling, respectively, show significant variability (McLennan et al. 1990). High-silica samples exhibit average Th/Sc and Zr/Sc ratios of 1.33 and 14.11 ppm, respectively, with ranges of 0.22–3.74 ppm for Th/Sc and 4.66–28.69 ppm for Zr/Sc. In contrast, low-silica samples display an average Th/Sc ratio of 1.40 and a Zr/Sc ratio of 16.97 ppm, but with extreme variability in their ranges (Th/Sc: 0.001–33.25 ppm; Zr/Sc: 1.22–423.33 ppm). The Th/Sc vs. Zr/Sc plot (Fig. S5c) reveals that both high-SiO_2 and low-SiO_2 metasedimentary averages align with UCC and PASS references, with no significant recycling.

The accumulation of heavy minerals, such as zircon, monazite, and/or allanite, during sediment transport contributes to the rise in normalized $(Gd/Yb)_{cn}$ values, which typically range between 1.0 and 2.0 ppm for post-Archean sediments and most upper crust igneous rocks (McLennan and Taylor 1991). Notably, Alutaguse high-SiO_2 samples exhibit an average $(Gd/Yb)_{cn}$ value of 4.58 ppm, while low-SiO_2 samples average 1.73 ppm, suggesting minimal heavy mineral fractionation and sediment recycling, with higher significance in high-SiO_2 samples. The significant negative Sr anomaly

in high-SiO_2 samples (Fig. 3d), compared to the low-SiO_2 counterpart (Fig. 3e), further underscores the limited recycled nature of these environments.

These observations underline the Alutaguse high-SiO_2 metasediments as highly sorted, reworked, and mature, in contrast to the geochemically immature low-SiO_2 samples.

6.2.3. Tectonic affinities

The tectonic environment of depositional basins and their geochemical characteristics are complexly related. The remaining sediments of derived sources can still provide valuable insights. However, studying tectonic settings requires caution, as sediments can cross boundaries (Chen et al. 2014). Several plots, initially designed for Phanerozoic clastic sediments, have been extended to Precambrian rock studies (El-Bialy 2013; Verma and Armstrong-Altrin 2013). However, relying solely on these plots can be misleading, as the elements used may be affected by processes such as sorting and mineral concentration (McLennan and Taylor 1991; El-Bialy 2013; Saccani 2015).

The elemental composition of sandstones, such as TiO_2, Al_2O_3, Fe_2O_3, and MgO concentrations, as well as Al_2O_3/SiO_2 ratios, varies across tectonic settings, transitioning from oceanic island arcs (OIA) to continental arcs, and further to active and passive continental margins (ACM, PCM; Bhatia 1983). Despite a wide range of values due to chemical mobility during weathering and diagenesis, the high TiO_2, Al_2O_3, Fe_2O_3, and MgO concentrations indicate that these sediments did not form in passive regimes (Bhatia and Crook 1986; McLennan and Taylor 1991).

Clastic sediments can be distinguished based on their K_2O/Na_2O and SiO_2 values, as shown by Roser and Korsch (1986; Fig. S5e), enabling differentiation between the PM, ACM, and ARC. Most Alutaguse metasediments align predominantly with the ACM. However, a few low-SiO_2 samples trend toward the ARC field. Some high-SiO_2 samples also overlap with the PM, but as Na and K are highly mobile, relying solely on Na_2O and K_2O for tectonic setting differentiation requires caution (El-Bialy 2013).

Verma and Armstrong-Altrin's (2013) discriminant-function-based multidimensional diagrams effectively distinguish between island/continental arcs, continental rifts, and collision settings, particularly for high-silica (SiO_2 >63 wt%) and low-silica rocks (SiO_2 < 63 wt%). The high-silica metasediments (Fig. 4d) predominantly align with the continental rift zone, a trend that is also consistent in the low-silica samples (Fig. 4e). Nevertheless, some low-SiO_2 graphite-bearing gneisses plot within the collision zone, possibly due to alteration patterns (i.e., LOI; Table S1).

Trace elements, such as Th, Sc, La, and Zr, are stable in depositional environments and serve as effective indicators for identifying source rocks (Bhatia and Crook 1986; Roser and Korsch 1986; McLennan et al. 1993). Bhatia and Crook (1986) employed these elements in Th–La–Sc and Sc–Th–Zr/10 triangular plots (Fig. 4f) to distinguish between four tectonic settings. These diagrams show that most Alutaguse metasediments align with the CIA zone, corroborated by their positioning relative to UCC and PAAS references. Notably, continental arcs and ACMs are similar, shaped by convergent plate dynamics, orogenic activity, and the evolution of subduction complexes (El-Bialy 2013).

The Alutaguse metasedimentary units display distinct geochemical signatures, such as a pronounced negative Eu anomaly, reduced Nb-Ta levels, dominant LREE patterns, and limited HREE fractionation (Fig. 3), suggesting a continental arc origin. However, as McLennan et al. (1990) note, specific geochemical markers do not conclusively determine tectonic settings, as the continental crust often exhibits arc-like characteristics. Nevertheless, the combined geochemical evidence supports a continental arc scenario for these units, with a potential back-arc context that is consistent with established tectonic models (All et al. 2004; Kirs et al. 2009; Bogdanova et al. 2015; Soesoo et al. 2020).

6.3. Metavolcanic rocks

6.3.1. The effects of shallow-level open-system processes

Shallow processes, such as crustal contamination, fractional crystallization, and post-magmatic alteration, can change the composition of mafic magma. Therefore, it is essential to consider these changes before using mafic igneous rocks to identify magma sources. For instance, the influence of crustal contamination on ascending magma is crucial, as it can cause chemical and isotopic variations in mafic magma. Typically, the continental crust exhibits enriched isotopic compositions and high SiO_2 content (Rudnick and Gao 2003).

The LOI values in the Alutaguse metavolcanic units range from 0.22 to 8.49 wt% (average 1.80 wt%; Table S1), indicating possible alterations caused by seawater or metamorphic fluids. This is further supported by carbonation patterns (Ma et al. 2021; Fig. S4d, e). Nevertheless, Figure S4e shows that the samples lie within or around the least-altered domain. The LOI values for 2-pyroxene gneiss samples are high (0.22–8.49 wt%; average 2.50 wt%). However, LOI values below 5 wt% generally do not show significant correlations with the abundances of fluid-mobile elements, such as Rb, Ba, Sr, U, Pb, K_2O, and particularly Zr and Nb, in mafic-ultramafic rocks (Pearce and Norry 1979; Saccani et al. 2018; Ma et al. 2021).

Bivariant Zr plots provide further insights into element mobility (Table S2). The effects of shallow-level open-system processes on the compositions of the studied metavolcanic rocks seem insignificant, providing valuable information on the composition of their magmatic origin and processes (Karakaş and Güçtekin 2021; Ma et al. 2021).

6.3.2. Crystallization and partial melting

The Alutaguse metavolcanic samples show tholeiitic tendencies (Fig. S3d). The predominantly subalkaline Zr underscores this distinction vs. Nb/Y ratios for most samples (Fig. S6a). These samples are also identified as metaluminous (Fig. 5a).

Major oxide relationships suggest fractional crystallization, influenced by ferromagnesian minerals (Yang et al. 2014; Ma et al. 2021; Fig. 2b). Metavolcanic units display MgO contents that are positively correlated with SiO_2 but inversely with Fe_2O_3 (Fig. 2b). Additionally, the Ni depletion

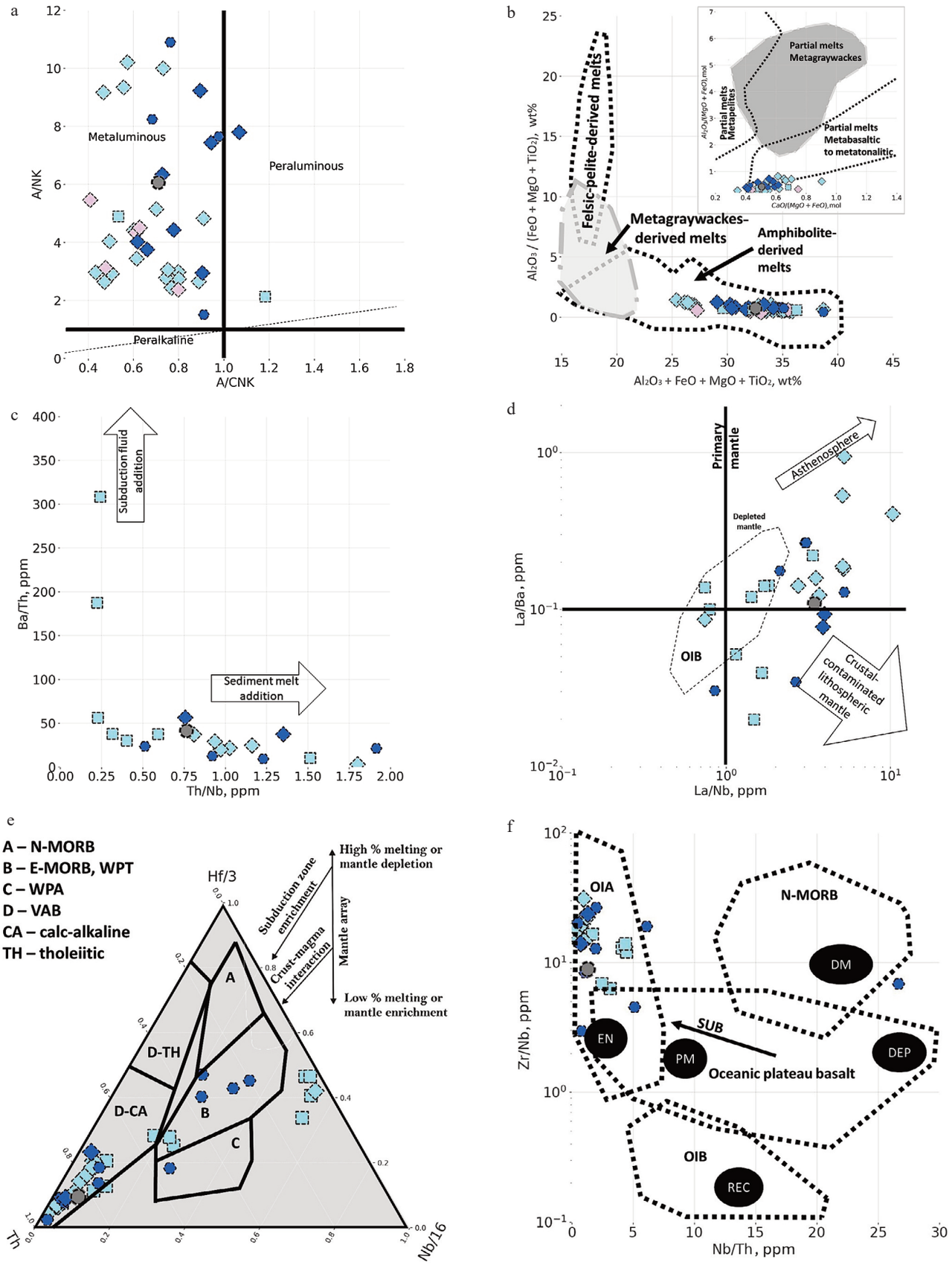

Fig. 5. Source and tectonic setting plots of Alutaguse metavolcanic samples: **a** – A/CNK (molar ratio of Al_2O_3 / ($CaO + Na_2O + K_2O$)) vs. A/NK (molar ratio of Al_2O_3 / ($Na_2O + K_2O$)) plot (after Shand 1943); **b** – Al_2O_3 / ($FeO + MgO + TiO_2$) vs. $Al_2O_3 + FeO + MgO + TiO_2$ plot (after Patiño Douce 1999), with an inset of Altherr et al. (2000) discrimination diagram Al / (Mg + Fe) vs. Ca / (Mg/Fe) (mol); **c** – Ba/Th vs. Th/Nb plot (after Saccani et al. 2018); **d** – La/Ba vs. La/Nb plot (after Hart 1988); **e** – Hf/3–Th–Nb/16 triangular plot (after Wood 1980); **f** – Nb/Th vs. Zr/Nb plot (after Condie 2005). Sample marker legend as shown in Figure 2b. Abbreviations: OIB – ocean island basalt, N-MORB – normal mid-ocean ridge basalt, E-MORB – enriched mid-ocean ridge basalt, WPT – within-plate tholeiite, WPA – within-plate alkaline basalt, VAB – volcanic arc-basalt, OIA – oceanic island arc, SUB – subduction zone, EN – enriched mantle, PM – primitive mantle, DM – depleted mantle, DEP – deep mantle, REC – recycled material.

(Fig. 3f) points to olivine fractional crystallization (Ma et al. 2021). Stable CaO/Al_2O_3 ratios, despite fluctuating MgO levels, indicate minimal clinopyroxene fractionation (Ma et al. 2021; Fig. 2b). The negative correlation of MgO with Al_2O_3, CaO, and Na_2O (Fig. 3c), along with minimal to slightly positive Eu anomalies (Eu/Eu*: 0.34–0.55; average 0.44; Fig. 3i), implies limited plagioclase fractionation (Floyd et al. 1989; Faisal et al. 2020). Sr enrichment is due to its rejection by most magmatic minerals, such as pyroxenes, instead favoring its incorporation into plagioclases (Faisal et al. 2020; Ma et al. 2021). The negative correlation between TiO_2 and MgO contents (Fig. 3c) suggests that the fractional crystallization of Ti-bearing minerals is negligible (Ma et al. 2021).

Experimental studies by Patiño Douce (1999) reveal compositional variations in melts derived from pelites, graywackes, and amphibolites, marked by differing Al concentrations. These variations arise from the dehydration melting of source rocks with distinct mineral compositions, which is particularly relevant in the context of crustal contamination. Pelite-derived melts, for instance, exhibit higher aluminum concentrations compared to those derived from psammites, and significantly more than those from amphibolites. This trend is observable in the Alutaguse metavolcanic samples, suggesting a strong pelitic influence in the source material (Fig. 5b). Furthermore, the discrimination diagram by Altherr et al. (2000), which plots Al / (Mg + Fe) vs. Ca / (Mg/Fe) (mol), supports the interpretation that the Alutaguse metavolcanics are primarily derived from metabasaltic to metatonalitic partial melts, indicating that the Alutaguse mantle-derived magmas share a provenance similar to amphibolite-basaltic crustal material or may have interacted with crustal material of this composition, rather than originating from metagraywackes or felsic (meta)pelites (Fig. 5b inset).

Elevated Nb and reduced Zr levels indicate mantle sources that vary from depleted to transitional (Pearce et al. 1996). Specifically, Nb levels below 10 ppm and Zr levels below 200 ppm characterize depleted mantle, whereas higher concentrations suggest transitional to enriched sources. In Alutaguse, the average concentrations of Nb and Zr are 10.23 and 90.75 ppm, respectively, positioning the region's samples primarily on the cusp of the transitional and depleted mantle domains, with a tendency toward the latter, as illustrated in the Nb vs. Zr plot (Fig. S6a).

The Nb/Y and Zr/Y ratios, known for their reliability in tracing melting and crystallization processes, help in identifying magma sources using the Fitton et al. (1997) δNb formula, defined as $\delta Nb = 1\log(Nb/Y) + 1.74 – (1.92\ (\log(Zr/Y))$. A δNb value greater than 0 indicates an enriched mantle, while a value less than 0 suggests a depleted source. Alutaguse metavolcanics exhibit δNb values ranging from –0.63 to 1.44, with an average of 0.25, highlighting significant heterogeneity. These values generally indicate an enriched mantle source, except for the pyroxene gneisses + amphibolites, which trend toward a depleted mantle (Table S2). La/Yb vs. Zr/Nb and La/Sm vs. Sm/Yb plots effectively illustrate melting trajectories from spinel and garnet-lherzolite, demonstrating mantle depletion and enrichment trends (Yang et al. 2014). The La/Yb vs. Zr/Nb plot (Fig. S6b) predominantly favors garnet-lherzolite melting patterns, while the La/Sm vs. Sm/Yb plot (Fig. S6c) shows samples closely following the spinel-lherzolite trend, approaching the PM reference. These patterns suggest that the parental magmas of the Alutaguse mafic metavolcanic rocks likely originated from high degrees of partial melting, approximately 30%, with a slight depletion trend. However, only three samples were analyzed using these relations (Table 2).

6.3.3. The nature of magma sources

The composition of mafic magmas is influenced by fractional crystallization and rock assimilation, which shape their elemental composition. However, trace element profiles, especially those of incompatible elements, are more reflective of the composition and melting degree of the mantle source. These profiles indicate distinct source characteristics specific to tectono-magmatic environments (Sifeta et al. 2005; Faisal et al. 2020; Ma et al. 2021). Determining magma sources and the degree of partial melting is pivotal and can be accomplished through the analysis of light REE and HFSE content and their ratios. Even amidst mineral accumulation or fractionation during mafic magmas' crystallization, LILE enrichment, HFSE depletion, and ratios of incompatible trace elements, such as Nb/Zr, Th/Zr, Ba/Th, U/Th, and Th/Nb, remain relatively consistent. These ratios are mainly influenced by the fractional crystallization of olivine, clinopyroxene, and plagioclase. Therefore, these elements arguably mirror the source's elemental ratios, even with moderate fractionation (Saccani et al. 2018; Wan et al. 2019; Ma et al. 2021).

The Alutaguse samples show elevated Th/Nb, Ba/Th (Fig. 5c), and U/Th ratios (Fig. S6d), as well as increased Th/Zr ratios (Fig. S6a), suggesting that their composition is primarily shaped by sedimentary melt processes rather than influence from subducted oceanic crust. The La/Ba vs. La/Nb plot (Fig. 5d) further supports the interpretation that the Alutaguse metavolcanics likely originate from an asthenospheric mantle source. This implies sedimentary melting activities (Fig. 5c) and indicates a mantle composition distinct from crust-contaminated sources, such as those found in the subduction-influenced southern Svecofennian domains of southern Finland (Lahtinen 2000; Kähkönen 2005; Kukkonen and Lauri 2009; Nironen 2017; Kara et al. 2021).

6.3.4. Tectonic setting implications

Debates on the tectonic origins of the analyzed metavolcanics have linked them to island arc collisions and rift mechanisms (Lahtinen 2000; Kirs et al. 2009; Bogdanova et al. 2015; Soesoo et al. 2020). HFSEs and HREEs, due to their stability, are critical for identifying the tectonic settings of extrusive rocks (Pearce et al. 1996; Sifeta et al. 2005; Saccani et al. 2018). Unlike typical mid-ocean ridge basalt (MORB) from asthenospheric mantle melting, which exhibits lower LREEs and LILEs, Alutaguse metavolcanics display an arc-like signature with notable HFSE depletion, suggesting subduction influences (Faisal et al. 2020; Ma et al. 2021). REE analysis shows that Alutaguse chondrite-normalized metavolcanics range from island arc basalts (IAB) to enriched mid-ocean

ridge basalt (E-MORB), significantly differing in LREE content from associated metasediments (Fig. 3i).

Geochemical plots, such as TiO_2–10(MnO)–10(P_2O_5) (Fig. S7a) and Y/15–La/10–Nb/8 (Fig. S7b), confirm that most samples from Alutaguse primarily fall within the island arc tholeiites (IAT) domain and the calc-alkaline basalts zone, indicative of a compressional arc setting. Furthermore, the Hf/3–Th–Nb/16 plot (Fig. 5e) positions these samples in the calc-alkaline volcanic arc-basalt (VAB) zone, suggesting a trend of crustal-magma interactions. Additional plots, such as log(Nb/Th) vs. log(Y/La) (Fig. S7c) and Nb/Th vs. Zr/Nb (Fig. S6a), show the Alutaguse samples aligning mainly with the arc domain. These positions notably reflect influences from the IAB and an arc-enriched component.

The Zr/Y vs. Zr plot (Fig. S6a), which differentiates between continental and oceanic basalts with a threshold value of 3, shows that while the samples mostly occupy the continental domain, they extend into the oceanic domain, particularly evident in the 2-pyroxene gneiss samples with high Y values (Table S2). Discrimination plots by Saccani (2015) reveal back-arc basin basalt (BABB) affinities, aligning with the assimilation-fractional crystallization (AFC) trend and spanning the oceanic subduction setting domain + rifted margin (Figs S6e, S7d).

6.4. Geodynamic implications

Although data are sparse, compelling evidence details a rich geological and tectonic history of the southern Fennoscandian Shield. This includes a major accretionary and collisional event during the late Svecofennian era, around 1.9–1.8 Ga, that amalgamated Sarmatia, Fennoscandia, and Volgo–Uralia into a single landmass (Bogdanova et al. 2006; Bogdanova et al. 2015; Nironen 2017; Pesonen et al. 2021; Lahtinen et al. 2022). Paleomagnetic studies and geological data have revealed a 2000 km-wide oceanic basin existing around 1.9 Ga, featuring island arcs and microcontinents, such as the Uusimaa and Bergslagen belts, which underscore complex subduction and collisional dynamics persisting until about 1.7 Ga (Korja et al. 1993; Claesson et al. 2001; Korja et al. 2003; Skridlaite et al. 2003; Lahtinen et al. 2005). In northern Estonia's Tallinn zone, metapelitic and metavolcanic gneisses dating between 2.13 and 1.85 Ga, along with the Uusimaa belt's 1.92–1.91 Ga felsic metavolcanic rocks, indicate subduction-related Paleoproterozoic crustal growth (Petersell and Levchenkov 1994; Puura et al. 2004; Bogdanova et al. 2015; Soesoo et al. 2020). These features, which resonate with the Bergslagen region's similar geological formations, suggest a unified geological structure across these belts (All et al. 2004; Puura et al. 2004; Kirs et al. 2009; Stephens and Weihed 2020). Moreover, West Estonian metapelitic rocks display detrital zircon ages ranging from 1.97 to 1.90 Ga, indicating a maximum deposition age of 1.90 Ga. This suggests proximity to the Bergslagen microcontinent and adjacent Svecofennian arcs as potential primary sources for sedimentation in the West Estonian basin (Kähkönen 2005; Bogdanova et al. 2015).

During 1.92–1.90 Ga, the concurrent formation of the Uusimaa and Tampere belts is hypothesized to have originated from distinct subduction-arc systems, likely due to a relatively shorter slab subducting beneath Bergslagen, as indicated by the older ages of the arc belts (Kukkonen and Lauri 2009; Bogdanova et al. 2015; Nironen 2017; Kara 2021). This theory supports the model of a subduction system forming the Uusimaa belt, as suggested by Kukkonen and Lauri (2009), and maintains the proposed timeline for the Tallinn–Uusimaa belt formations around 1.92–1.90 Ga (Fig. 6a).

From 1.91 to 1.80 Ga, persistent lithospheric convergence hindered the gravitational collapse of the over-thickened crust. Evidence of this includes a 50 km-thick crust in central Finland and Estonia (Korja et al. 1993, 2003; Solano-Acosta et al. 2023). This era saw Sarmatia, Fennoscandia, and Volgo–Uralia merging, forming a vast landmass via accretionary and collisional dynamics. Prevalent arc-type magmatism around 1.90 to 1.89 Ga offers insights into the region's geodynamic evolution (Kähkönen 2005; Kara et al. 2021). The Bergslagen region reveals back-arc rifting events and associated granitoid magmatism and sedimentation until approximately 1.85 Ga. Geological correlations between the Swedish Skellefte district and the Tampere and Pirkanmaa belts highlight intricate magmatic and tectonic interactions (Allen et al. 1996; Beunk and Kuipers 2012; Bogdanova et al. 2015; Nironen 2017; Stephens and Weihed 2020; Kara et al. 2021).

Between 1.90 and 1.88 Ga, the Tallinn–Uusimaa belt(s) experienced sedimentation intermixed with volcanic activity, suggesting a shared origin with Alutaguse metasediments due to similar CaO and MnO enrichments (Kivisilla et al. 1999; Rasilainen et al. 2007; Kirs et al. 2009; Kukkonen and Lauri 2009; Bogdanova et al. 2015; Nironen 2017; Lahtinen et al. 2022; Fig. 6). The Alutaguse metavolcanics, influenced by asthenospheric magmatism (Fig. 5), contrast the southern Svecofennian Finnish domains, which show significant crustal interactions from subduction (Kukkonen and Lauri 2009; Kara 2021; Lahtinen et al. 2022). By 1.89 Ga, the Alutaguse zone was characterized as a back-arc area (Kirs et al. 2009; Bogdanova et al. 2015; Soesoo et al. 2020; Fig. 6b), followed by sedimentation in a back-arc rift system (Fig. 4). The 1.89 Ga Jõhvi units displayed a magmatic-magnetite peak, indicative of mantle uplift during Alutaguse rifting (Bogdanova et al. 2015; Nirgi and Soesoo 2021).

Figure 6c depicts the progressive collision of Bergslagen and its subsequent formations between 1.89–1.87 Ga (Bogdanova et al. 2015; Nironen 2017). In the South Estonian domain (SEG), during this same period, the crystallization of garnet–orthopyroxene granodiorite and subsequent deformation and migmatization by 1.86 Ga suggest an extensional back-arc scenario, likely initiating the Middle Estonian fault zone (MEFZ) and regional granulite-facies metamorphism (Kirs et al. 2009; Bogdanova et al. 2015; Soesoo et al. 2020). This phase aligns with broader regional tectonic processes, underscoring the dynamic geological evolution of these domains during the Proterozoic.

Between 1.87 and 1.86 Ga, the Bergslagen microcontinent collided with the Svecofennian arc, leading to the formation of calc-alkaline granitoids (Kähkönen 2005; Nironen 2017; Mikkola et al. 2018; Kara et al. 2021). Subsequent intra-orogenic sedimentary basins developed in southern Finland

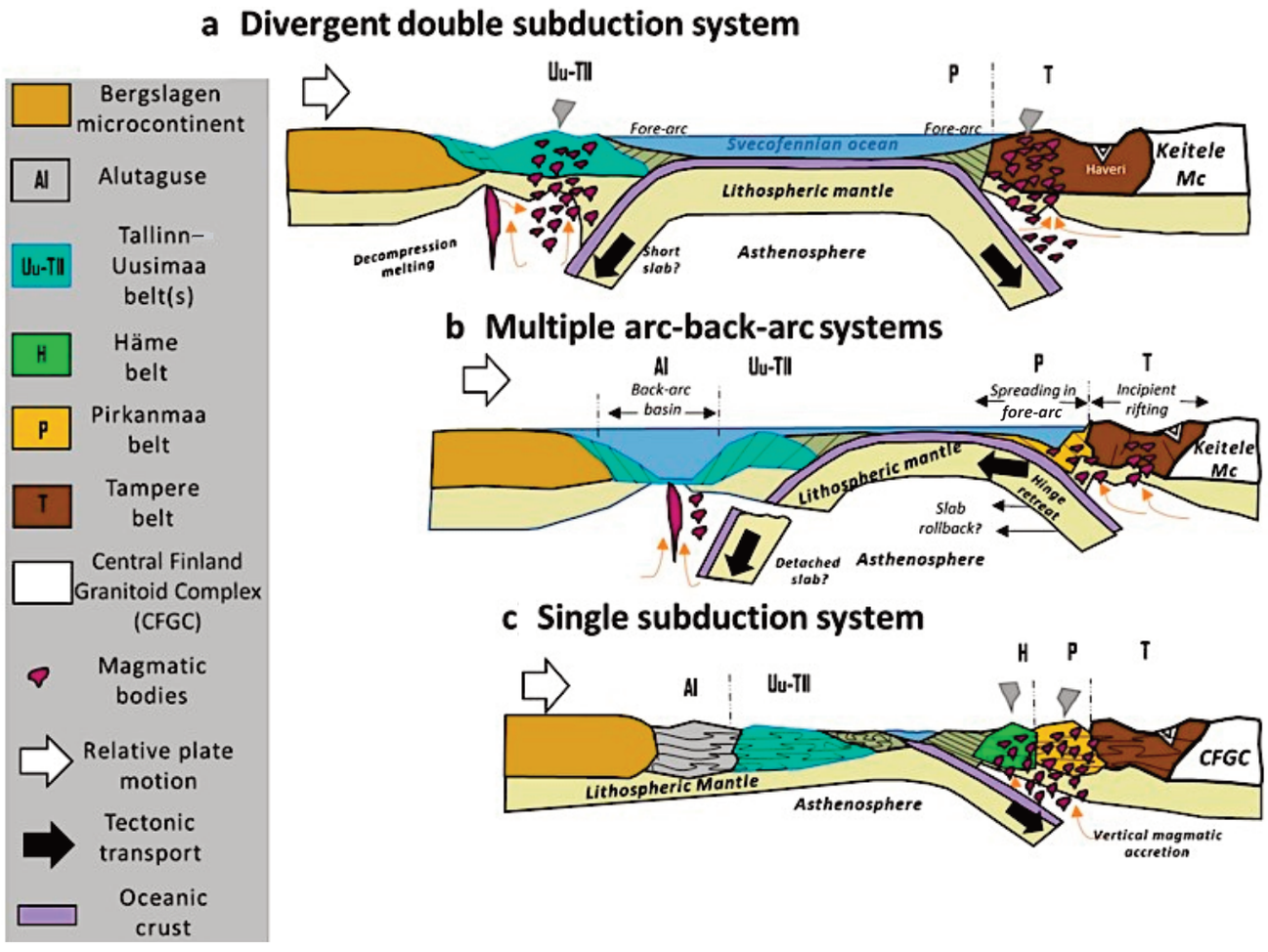

Fig. 6. Schematic geodynamic model (after Kukkonen and Lauri 2009; Kara et al. 2021) of the evolution of Fennoscandia during: **a** – 1.92–1.90 Ga, **b** – 1.90–1.89 Ga, **c** – 1.89–1.87 Ga. The model is a conceptual, not-to-scale representation, designed to illustrate key dynamics rather than precise physical dimensions.

between 1.86 and 1.83 Ga, following granitoid emplacement and preceding late-orogenic granites (Lahtinen et al. 2002, 2005, 2008, 2009; Lahtinen and Nironen 2010; Lahtinen et al. 2011; Nironen 2017). During this period, NW-directed convergence involved the Häme belt in the north and the Uusimaa belt in the south, culminating in the closure of the paleo-Svecofennian ocean (Kukkonen and Lauri 2009; Kara et al. 2021). This collision may be associated with collisional signals observed in a few metasediments, particularly those with low silica content (Fig. 4e). By 1.86 Ga, the geological similarities in the Häme and Uusimaa belts, as reflected in the trace elements of their metasediments, indicate a shared geodynamic evolution since then (Kukkonen and Lauri 2009; Nironen 2017; Kara et al. 2021).

7. Conclusions

This study has advanced the understanding of the metasedimentary and metavolcanic rocks in the Alutaguse zone by compiling historical geochemical data and integrating new samples, offering a refined perspective on the zone's geological evolution and its relation to the Svecofennian orogeny formations across Fennoscandia. The high-SiO_2 metasediments, resembling litharenites, show signs of extensive reworking and alignment with continental rift zones, indicative of a dynamic geological history and a mature sedimentary environment. In contrast, the low-SiO_2 samples indicate a more complex, collisional tectonic setting with significant hydrothermal alterations, suggesting mafic to intermediate origins and limited sediment reworking. The metavolcanic units analyzed in this study are characterized by subalkaline, tholeiitic trends, metaluminous characteristics, and asthenospheric mantle origins, underscoring a compressional arc environment.

The study's findings suggest that the Alutaguse zone has rift origins and is genetically linked to the Uusimaa units. This supports a double subduction collision model for Fennoscandia's evolution around 1.92–1.87 Ga. Further investigation is needed to determine whether the Tallinn zone is affiliated with the Uusimaa belt or represents a distinct arc predating Uusimaa. The study emphasizes the importance of geochronological assessments, specifically U–Pb isotopic dating of zircon and garnet samples, to refine the provenance of metasedimentary rocks and explore Zn-Pb-Cu anomalies associated with rift-related deposits in the Bergslagen region. Additionally, detailed analysis of sulfurized gneisses could enhance the understanding of local metallogenesis in areas with significant metalliferous anomalies. Finally, detailed gravimetric and magnetic surveys across the Alutaguse zone are essential to map geophysical anomalies and their potential links to metal-bearing deposits.

Data availability statement

Data not already included in the paper and its supplementary materials will be made available upon request.

Acknowledgments

This research was supported by the DEXPLORE Horizon Research Funds (document No. VHE24051) and funded through the Horizon Europe program HORIZON-CL4-2024-RESILIENCE-01-01. Research was partly funded by the Estonian Research Council's project TemTA-30. We also thank the EU Funding and Tenders Portal for its support under project ID No. 101178897. Special thanks to the peer reviewers for their thoughtful comments, feedback, and suggestions. The publication costs of this article were partially covered by the Estonian Academy of Sciences.

Supplementary online data

Supplementary online data to this article can be found at https://doi.org/10.3176/earth.2025.S05. The supplementary material is designed to provide an in-depth analysis, including the complete analyzed geochemical dataset of the Alutaguse zone.

References

All, T., Puura, V. and Vaher, R. 2004. Orogenic structures of the Precambrian basement of Estonia as revealed from the integrated modelling of the crust. In *Proceedings of the Estonian Academy of Sciences, Geology*, **53**(3), 165–189. https://doi.org/10.3176/geol.2004.3.03

Allen, R. L., Lundstrom, I., Ripa, M. and Christofferson, H. 1996. Facies analysis of a 1.9 Ga, continental margin, back-arc, felsic caldera province with diverse Zn-Pb-Ag-(Cu-Au) sulfide and Fe oxide deposits, Bergslagen region, Sweden. *Economic Geology*, **91**(6), 979–1008. https://doi.org/10.2113/gsecongeo.91.6.979

Altherr, R., Holl, A., Hegner, E., Langer, C. and Kreuzer, H. 2000. High-potassium, calc-alkaline I-type plutonism in the European Variscides: northern Vosges (France) and northern Schwarzwald (Germany). *Lithos*, **50**(1–3), 51–73. https://doi.org/10.1016/S0024-4937(99)00052-3

Armstrong-Altrin, J., Lee, Y. I., Verma, S. P. and Ramasamy, S. 2004. Geochemistry of sandstones from the Upper Miocene Kudankulam Formation, southern India: implications for provenance, weathering, and tectonic setting. *Journal of Sedimentary Research*, **74**(2), 285–297. https://doi.org/10.1306/082803740285

Bailie, R., Gutzmer, J. and Rajesh, H. M. 2011. Petrography, geochemistry and geochronology of the metavolcanic rocks of the Mesoproterozoic Leerkrans Formation, Wilgenhoutsdrif Group, South Africa – back-arc basin to the Areachap volcanic arc. *South African Journal of Geology*, **114**(2), 167–194. https://doi.org/10.2113/gssajg.114.2.167

Baltybaev, S. K. 2013. Svecofennian orogen of the Fennoscandian Shield: compositional and isotopic zoning and its tectonic interpretation. *Geotectonics*, **47**(6), 452–464. https://doi.org/10.1134/S0016852113060022

Beunk, F. F. and Kuipers, G. 2012. The Bergslagen ore province, Sweden: review and update of an accreted orocline, 1.9–1.8 Ga BP. *Precambrian Research*, **216–219**, 95–119. https://doi.org/10.1016/j.precamres.2012.05.007

Bhatia, M. R. 1983. Plate tectonics and geochemical composition of sandstones. *The Journal of Geology*, **91**(6), 611–627. https://doi.org/10.1086/628815

Bhatia, M. R. and Crook, K. A. W. 1986. Trace element characteristics of graywackes and tectonic setting discrimination of sedimentary basins. *Contributions to Mineralogy and Petrology*, **92**(2), 181–193. https://doi.org/10.1007/BF00375292

Bogdanova, S., Gorbatschev, R., Grad, M., Janik, T., Guterch, A., Kozlovskaya, E. et al. 2006. EUROBRIDGE: new insight into the geodynamic evolution of the East European Craton. *Geological Society, London, Memoirs*, **32**(1), 599–625. https://doi.org/10.1144/GSL.MEM.2006.032.01.36

Bogdanova, S., Gorbatschev, R., Skridlaite, G., Soesoo, A., Taran, L. and Kurlovich, D. 2015. Trans-Baltic Palaeoproterozoic correlations towards the reconstruction of supercontinent Columbia/Nuna. *Precambrian Research*, **259**, 5–33. https://doi.org/10.1016/j.precamres.2014.11.023

Casey, J. F., Banerji, D. and Zarian, P. 2007. Leg 179 synthesis: geochemistry, stratigraphy, and structure of gabbroic rocks drilled in ODP Hole 1105a, Southwest Indian Ridge. In *Proceedings of the Ocean Drilling Program, Scientific Results*, Vol. 179 (Casey, J. F. and Miller, D. J., eds). College Station, Texas, 1–125. https://doi.org/10.2973/odp.proc.sr.179.001.2007

Chaudhuri, S. and Cullers, R. L. 1979. The distribution of rare-earth elements in deeply buried Gulf Coast sediments. *Chemical Geology*, **24**(3–4), 327–338. https://doi.org/10.1016/0009-2541(79)90131-1

Chen, M., Sun, M., Cai, K., Buslov, M. M., Zhao, G. and Rubanova, E. S. 2014. Geochemical study of the Cambrian–Ordovician meta-sedimentary rocks from the northern Altai-Mongolian terrane, northwestern Central Asian Orogenic Belt: implications on the provenance and tectonic setting. *Journal of Asian Earth Sciences*, **96**, 69–83. https://doi.org/10.1016/j.jseaes.2014.08.028

Claesson, S., Bogdanova, S., Bibikova, E. and Gorbatschev, R. 2001. Isotopic evidence for Palaeoproterozoic accretion in the basement of the East European Craton. *Tectonophysics*, **339**(1–2), 1–18. https://doi.org/10.1016/S0040-1951(01)00031-2

Condie, K. C. 1993. Chemical composition and evolution of the upper continental crust: contrasting results from surface samples and shales. *Chemical Geology*, **104**(1–4), 1–37. https://doi.org/10.1016/0009-2541(93)90140-E

Condie, K. C. 2005. High field strength element ratios in Archean basalts: a window to evolving sources of mantle plumes? *Lithos*, **79**(3–4), 491–504. https://doi.org/10.1016/j.lithos.2004.09.014

Cox, R., Lowe, D. R. and Cullers, R. 1995. The influence of sediment recycling and basement composition on evolution of mudrock chemistry in the southwestern United States. *Geochimica et Cosmochimica Acta*, **59**(14), 2919–2940. https://doi.org/10.1016/0016-7037(95)00185-9

Cullers, R. L. 1994. The controls on the major and trace element variation of shales, siltstones, and sandstones of Pennsylvanian-Permian age from uplifted continental blocks in Colorado to platform sediment in Kansas, USA. *Geochimica et Cosmochimica Acta*, **58**(22), 4955–4972. https://doi.org/10.1016/0016-7037(94)90224-0

Cullers, R. L., Bock, B. and Guidotti, C. 1997. Elemental distributions and neodymium isotopic compositions of Silurian metasediments, western Maine, USA: redistribution of the rare earth elements. *Geochimica et Cosmochimica Acta*, **61**(9), 1847–1861. https://doi.org/10.1016/S0016-7037(97)00048-3

de Carvalho Mendes, L., dos Santos, T. J. S. and Gomes, N. B. 2021. Geochemistry and provenance of the metasedimentary rocks surrounding the Santa Quitéria magmatic arc, NE Brazil: tectonic and paleogeographic implications for the assembly of West Gondwana. *Precambrian Research*, **356**, 106063. https://doi.org/10.1016/j.precamres.2020.106063

El-Bialy, M. Z. 2013. Geochemistry of the Neoproterozoic metasediments of Malhaq and Um Zariq formations, Kid metamorphic complex, Sinai, Egypt: implications for source-area weathering, provenance, recycling, and depositional tectonic setting. *Lithos*, **175–176**, 68–85. https://doi.org/10.1016/j.lithos.2013.05.002

Faisal, M., Yang, X., Khalifa, I. H., Amuda, A. K. and Sun, C. 2020. Geochronology and geochemistry of Neoproterozoic Hamamid metavolcanics hosting largest volcanogenic massive sulfide deposits in Eastern Desert of Egypt: implications for petrogenesis and tectonic evolution. *Precambrian Research*, **344**, 105751. https://doi.org/10.1016/j.precamres.2020.105751

Fedo, C. M., Nesbitt, H. W. and Young, G. M. 1995. Unraveling the effects of potassium metasomatism in sedimentary rocks and paleosols, with implications for paleoweathering conditions and provenance. *Geology*, **23**(10), 921–924. https://doi.org/10.1130/0091-7613(1995)023%3C0921:UTEOPM%3E2.3.CO;2

Fedo, C. M., Eriksson, K. A. and Krogstad, E. J. 1996. Geochemistry of shales from the Archean (~3.0 Ga) Buhwa Greenstone Belt, Zimbabwe: implications for provenance and source-area weathering. *Geochimica et Cosmochimica Acta*, **60**(10), 1751–1763. https://doi.org/10.1016/0016-7037(96)00058-0

Feng, R. and Kerrich, R. 1990. Geochemistry of fine-grained clastic sediments in the Archean Abitibi greenstone belt, Canada: implications for provenance and tectonic setting. *Geochimica et Cosmochimica Acta*, **54**(4), 1061–1081. https://doi.org/10.1016/0016-7037(90)90439-R

Fitton, J. G., Saunders, A. D., Norry, M. J., Hardarson, B. S. and Taylor, R. N. 1997. Thermal and chemical structure of the Iceland plume. *Earth and Planetary Science Letters*, **153**(3–4), 197–208. https://doi.org/10.1016/S0012-821X(97)00170-2

Floyd, P. A., Winchester, J. A. and Park, R. G. 1989. Geochemistry and tectonic setting of Lewisian clastic metasediments from the Early Proterozoic Loch Maree Group of Gairloch, NW Scotland. *Precambrian Research*, **45**(1–3), 203–214. https://doi.org/10.1016/0301-9268(89)90040-5

Gao, S. and Wedepohl, K. H. 1995. The negative Eu anomaly in Archean sedimentary rocks: implications for decomposition, age and importance of their granitic sources. *Earth and Planetary Science Letters*, **133**(1–2), 81–94. https://doi.org/10.1016/0012-821X(95)00077-P

Gao, S., Ling, W., Qiu, Y., Lian, Z., Hartmann, G. and Simon, K. 1999. Contrasting geochemical and Sm-Nd isotopic compositions of Archean metasediments from the Kongling high-grade terrain of the Yangtze craton: evidence for cratonic evolution and redistribution of REE during crustal anatexis. *Geochimica et Cosmochimica Acta*, **63**(13–14), 2071–2088. https://doi.org/10.1016/S0016-7037(99)00153-2

Garcia, D., Fonteilles, M. and Moutte, J. 1994. Sedimentary fractionations between Al, Ti, and Zr and the genesis of strongly peraluminous granites. *The Journal of Geology*, **102**(4), 411–422. https://doi.org/10.1086/629683

Gu, X. X., Liu, J. M., Zheng, M. H., Tang, J. X. and Qi, L. 2002. Provenance and tectonic setting of the Proterozoic turbidites in Hunan, South China: geochemical evidence. *Journal of Sedimentary Research*, **72**(3), 393–407. https://doi.org/10.1306/081601720393

Han, Z.-Z., Zhong, W.-J., Song, Z.-G., Han, C., Han, M., Gao, L.-H. et al. 2019. Geochronology and geochemistry of metasedimentary rocks from the Dongnancha Formation in the Huadian area, central Jilin Province, Northeast (NE) China: implications for the tectonic evolution of the eastern segment of the Paleo-Asian Ocean. *Geochemistry*, **79**(1), 94–112. https://doi.org/10.1016/j.geoch.2018.12.002

Harker, A. 1909. *The Natural History of Igneous Rocks*. Macmillan, New York.

Harnois, L. 1988. The CIW index: a new chemical index of weathering. *Sedimentary Geology*, **55**(3–4), 319–322. https://doi.org/10.1016/0037-0738(88)90137-6

Hart, S. R. 1988. Heterogeneous mantle domains: signatures, genesis and mixing chronologies. *Earth and Planetary Science Letters*, **90**(3), 273–296. https://doi.org/10.1016/0012-821X(88)90131-8

Hayashi, K.-I., Fujisawa, H., Holland, H. D. and Ohmoto, H. 1997. Geochemistry of ~1.9 Ga sedimentary rocks from northeastern Labrador, Canada. *Geochimica et Cosmochimica Acta*, **61**(19), 4115–4137. https://doi.org/10.1016/S0016-7037(97)00214-7

Herron, M. M. 1988. Geochemical classification of terrigenous sands and shales from core or log data. *Journal of Sedimentary Research*, **58**(5), 820–829. https://doi.org/10.1306/212F8E77-2B24-11D7-8648000102C1865D

Ishikawa, Y., Sawaguchi, T., Iwaya, S. and Horiushi, M. 1976. Delineation of prospecting targets for Kuroko deposits based on modes of volcanism of underlying dacite and alteration haloes. *Mining Geology*, **26**(136), 105–117. https://doi.org/10.11456/shigenchishitsu1951.26.105

Jensen, L. S. 1976. *A New Cation Plot for Classifying Subalkalic Volcanic Rocks*, Vol. 66. Ministry of Natural Resources, Toronto.

Jian, X., Guan, P., Zhang, W. and Feng, F. 2013. Geochemistry of Mesozoic and Cenozoic sediments in the northern Qaidam Basin, northeastern Tibetan Plateau: implications for provenance and weathering. *Chemical Geology*, **360–361**, 74–88. https://doi.org/10.1016/j.chemgeo.2013.10.011

Kähkönen, Y. 2005. Svecofennian supracrustal rocks. In *Developments in Precambrian Geology*, Vol. 14 (Lehtinen, M., Nurmi, P. A. and Rämö, O. T., eds). Elsevier, 343–405. https://doi.org/10.1016/S0166-2635(05)80009-X

Kara, J. 2021. *Evolution of the Svecofennian bedrock in southern Finland: spatial and temporal changes in the mantle-derived magmatism and mantle-crust interaction.* PhD thesis. University of Turku, Finland.

Kara, J., Leskelä, T., Väisänen, M., Skyttä, P., Lahaye, Y., Tiainen, M. and Leväniemi, H. 2021. Early Svecofennian rift-related magmatism: geochemistry, U-Pb-Hf zircon isotope data and tectonic setting of the Au-hosting Uunimäki gabbro, SW Finland. *Precambrian Research*, **364**, 106364. https://doi.org/10.1016/j.precamres.2021.106364

Karakaş, A. and Güçtekin, A. 2021. Evaluation of physico-mechanical properties with petrographic characteristics of Hisartepe volcanic rocks (Söke-western Anatolia) based on alteration indices. *Arabian Journal of Geosciences*, **14**(12), 1117. https://doi.org/10.1007/s12517-021-07086-3

Kirs, J. and Petersell, V. 1994. Age and geochemical character of plagiomicrocline granite veins in the Abja gabbrodioritic massif. *Acta et Commentationes Universitatis Tartuensis*, **972**, 3–15.

Kirs, J., Puura, V., Soesoo, A., Klein, V., Konsa, M., Koppelmaa, H. et al. 2009. The crystalline basement of Estonia: rock complexes of the Palaeoproterozoic Orosirian and Statherian and Mesoproterozoic Calymmian periods, and regional correlations. *Estonian Journal of Earth Sciences*, **58**(4), 219–228. http://dx.doi.org/10.3176/earth.2009.4.01

Kivisilla, J., Niin, M. and Koppelmaa, H. 1999. *Catalogue of Chemical Analyses of Major Elements in the Rocks of the Crystalline Basement of Estonia*. Geological Survey of Estonia, Tallinn.

Klein, V. 1986. *Метаморфический комплекс свекофеннского пояса в Северной Эстонии (Metamorphic Complex of the Svecofennian Belt in Northern Estonia)*. PhD thesis. Leningrad State University, Russia.

Korja, A., Korja, T., Luosto, U. and Heikkinen, P. 1993. Seismic and geoelectric evidence for collisional and extensional events in the Fennoscandian Shield: implications for Precambrian crustal evolution. *Tectonophysics*, **219**(1–3), 129–152. https://doi.org/10.1016/0040-1951(93)90292-R

Korja, A., Lahtinen, R., Heikkinen, P., Kukkonen, I. and Fire Working Group. 2003. A tectonic model for Paleoproterozoic crocodile structures at Karelian Svecofennian boundary – results from FIRE-1 and BABEL2 & 3. In *EGS-AGU-EUG Joint Assembly, Abstracts from the meeting held in Nice, France, 6–11 April 2003*, abstract id. 2801.

Kukkonen, I. and Lauri, L. 2009. Modelling the thermal evolution of a collisional Precambrian orogen: high heat production migmatitic granites of southern Finland. *Precambrian Research*, **168**(3–4), 233–246. https://doi.org/10.1016/j.precamres.2008.10.004

Lahtinen, R. 2000. Archaean–Proterozoic transition: geochemistry, provenance and tectonic setting of metasedimentary rocks in central Fennoscandian Shield, Finland. *Precambrian Research*, **104**(3–4), 147–174. https://doi.org/10.1016/S0301-9268(00)00087-5

Lahtinen, R. and Nironen, M. 2010. Paleoproterozoic lateritic paleosol–ultra-mature/mature quartzite–meta-arkose successions in southern Fennoscandia – intra-orogenic stage during the Svecofennian orogeny. *Precambrian Research*, **183**(4), 770–790. https://doi.org/10.1016/j.precamres.2010.09.006

Lahtinen, R., Huhma, H. and Kousa, J. 2002. Contrasting source components of the Paleoproterozoic Svecofennian metasediments: detrital zircon U–Pb, Sm–Nd and geochemical data. *Precambrian Research*, **116**(1–2), 81–109. https://doi.org/10.1016/S0301-9268(02)00018-9

Lahtinen, R., Korja, A. and Nironen, M. 2005. Paleoproterozoic tectonic evolution. In *Developments in Precambrian Geology*, Vol. 14 (Lehtinen, M., Nurmi, P. A. and Rämö, O. T., eds). Elsevier, 481–531. https://doi.org/10.1016/S0166-2635(05)80012-X

Lahtinen, R., Garde, A. A. and Melezhik, V. A. 2008. Paleoproterozoic evolution of Fennoscandia and Greenland. *Episodes: Journal of International Geoscience*, **31**(1), 20–28. https://doi.org/10.18814/epiiugs/2008/v31i1/004

Lahtinen, R., Korja, A., Nironen, M. and Heikkinen, P. 2009. Palaeoproterozoic accretionary processes in Fennoscandia. *Geological Society, London, Special Publications*, **318**(1), 237–256. https://doi.org/10.1144/SP318.8

Lahtinen, R., Huhma, H., Kontinen, A., Kohonen, J. and Sorjonen-Ward, P. 2010. New constraints for the source characteristics, deposition and age of the 2.1–1.9 Ga metasedimentary cover at the western margin of the Karelian Province. *Precambrian Research*, **176**(1–4), 77–93. https://doi.org/10.1016/j.precamres.2009.10.001

Lahtinen, R., Hölttä, P., Kontinen, A., Niiranen, T., Nironen, M., Saalmann, K. and Sorjonen-Ward, P. 2011. Tectonic and metallogenic evolution of the Fennoscandian shield: key questions with emphasis on Finland. *Geological Survey of Finland, Special Paper*, **49**, 23–33.

Lahtinen, R., Huhma, H., Sipilä, P. and Vaarma, M. 2017. Geochemistry, U-Pb geochronology and Sm-Nd data from the Paleoproterozoic Western Finland supersuite – a key component in the coupled Bothnian oroclines. *Precambrian Research*, **299**, 264–281. https://doi.org/10.1016/j.precamres.2017.07.025

Lahtinen, R., Salminen, P. E., Sayab, M., Huhma, H., Kurhila, M. and Johnston, S. T. 2022. Age and structural constraints on the tectonic evolution of the Paleoproterozoic Saimaa orocline in Fennoscandia. *Precambrian Research*, **369**, 106477. https://doi.org/10.1016/j.precamres.2021.106477

Large, R. R., Gemmell, J. B., Paulick, H. and Huston, D. L. 2001. The alteration box plot: a simple approach to understanding the relationship between alteration mineralogy and lithogeochemistry associated with volcanic-hosted massive sulfide deposits. *Economic Geology*, **96**(5), 957–971. https://doi.org/10.2113/gsecongeo.96.5.957

Le Bas, M. J., Le Maitre, R. W., Streckeisen, A. and Zanettin, B. 1986. A chemical classification of volcanic rocks based on the total alkali-silica diagram. *Journal of Petrology*, **27**(3), 745–750. https://doi.org/10.1093/petrology/27.3.745

Ma, L.-T., Dai, L.-Q., Zheng, Y.-F., Zhao, Z.-F., Fang, W., Zhao, K. et al. 2021. Geochemical distinction between altered oceanic basalt- and seafloor sediment-derived fluids in the mantle source of mafic igneous rocks in southwestern Tianshan, western China. *Journal of Petrology*, **62**(1), egab014. https://doi.org/10.1093/petrology/egab014

MacLean, W. and Hoy, L. D. 1991. Geochemistry of hydrothermally altered rocks at the Horne Mine, Noranda, Quebec. *Economic Geology*, **86**(3), 506–528. https://doi.org/10.2113/gsecongeo.86.3.506

McDonough, W. F. and Frey, F. A. 1989. Rare earth elements in upper mantle rocks. In *Geochemistry and Mineralogy of Rare Earth Elements* (Lipin, B. R. and McKay, G. A., eds). De Gruyter, Berlin, Boston, 99–145. https://doi.org/10.1515/9781501509032-008

McLennan, S. M. 1989. Rare earth elements in sedimentary rocks: influence of provenance and sedimentary processes. In *Geochemistry and Mineralogy of Rare Earth Elements* (Lipin, B. R. and McKay, G. A., eds). De Gruyter, Berlin, Boston, 169–200. https://doi.org/10.1515/9781501509032-010

McLennan, S. M. 1993. Weathering and global denudation. *The Journal of Geology*, **101**(2), 295–303. https://doi.org/10.1086/648222

McLennan, S. M. 2001. Relationships between the trace element composition of sedimentary rocks and upper continental crust. *Geochemistry, Geophysics, Geosystems*, **2**(4). https://doi.org/10.1029/2000GC000109

McLennan, S. M. and Taylor, S. R. 1991. Sedimentary rocks and crustal evolution: tectonic setting and secular trends. *The Journal of Geology*, **99**(1), 1–21. https://doi.org/10.1086/629470

McLennan, S. M., Taylor, S. R., McCulloch, M. T. and Maynard, J. B. 1990. Geochemical and Nd-Sr isotopic composition of deep-sea turbidites: crustal evolution and plate tectonic associations. *Geochimica et Cosmochimica Acta*, **54**(7), 2015–2050. https://doi.org/10.1016/0016-7037(90)90269-Q

McLennan, S. M., Hemming, S. R., McDaniel, D. K. and Hanson, G. N. 1993. Geochemical approaches to sedimentation, provenance, and tectonics. In *Processes Controlling the Composition of Clastic Sediments* (Johnsson, M. J. and Basu, A., eds). Geological Society of America, Boulder, Colorado, 21–40. https://doi.org/10.1130/SPE284-p21

McLennan, S. M., Hemming, S. R., Taylor, S. R. and Eriksson, K. A. 1995. Early Proterozoic crustal evolution: geochemical and Nd–Pb isotopic evidence from metasedimentary rocks, southwestern North America. *Geochimica et Cosmochimica Acta*, **59**(6), 1153–1177. https://doi.org/10.1016/0016-7037(95)00032-U

Mikkola, P., Mönkäre, K., Ahven, M. and Huhma, H. 2018. Geochemistry and age of the Paleoproterozoic Makkola suite volcanic rocks in central Finland. In *Development of the Paleoproterozoic Svecofennian Orogeny: New Constraints from the Southeastern Boundary of the Central Finland Granitoid Complex* (Mikkola, P., Hölttä, P. and Käpyaho, A., eds). Geological Survey of Finland, Bulletin, **407**, 85–105. http://doi.org/10.30440/bt407.5

Nesbitt, H. W. and Young, G. M. 1982. Early Proterozoic climates and plate motions inferred from major element chemistry of lutites. *Nature*, **299**, 715–717. https://doi.org/10.1038/299715a0

Nirgi, S. and Soesoo, A. 2021. Geology and geochemistry of a Paleoproterozoic iron mineralization in North-Eastern Estonia. *Proceedings of the Karelian Research Centre of the Russian Academy of Sciences*, **10**, 25–43. https://doi.org/10.17076/geo1492

Nironen, M. 2017. *Bedrock of Finland at the Scale 1:1000000 – Major Stratigraphic Units, Metamorphism and Tectonic Evolution*. Geological Survey of Finland, Espoo.

Parker, A. 1970. An index of weathering for silicate rocks. *Geological Magazine*, **107**(6), 501–504. https://doi.org/10.1017/S0016756800058581

Patiño Douce, A. E. 1999. What do experiments tell us about the relative contributions of crust and mantle to the origin of granitic magmas? *Geological Society, London, Special Publications*, **168**(1), 55–75. https://doi.org/10.1144/GSL.SP.1999.168.01.05

Pearce, J. A. 1996. A user's guide to basalt discrimination diagrams. In *Trace Element Geochemistry of Volcanic Rocks: Applications for Massive Sulphide Exploration* (Wyman, D. A., ed.). Geological Association of Canada, St. John's, 79–113.

Pearce, J. A. and Norry, M. J. 1979. Petrogenetic implications of Ti, Zr, Y, and Nb variations in volcanic rocks. *Contributions to Mineralogy and Petrology*, **69**(1), 33–47. https://doi.org/10.1007/BF00375192

Pesonen, L. J., Salminen, J., Elming, S.-Å., Evans, D. A. D. and Veikkolainen, T. 2021. *Ancient Supercontinents and the Paleo-*

geography of Earth. Elsevier, Amsterdam. https://doi.org/10.1016/C2018-0-03855-4

Petersell, V. and Levchenkov, O. 1994. On the geological structure of the crystalline basement of the southern slope of the Baltic Shield. *Acta et Commentationes Universitatis Tartuensis*, **972**(14), 16–39.

Pettijohn, F. J., Potter, P. E. and Siever, R. 1987. Sedimentary structures and bedding. In *Sand and Sandstone*. Springer, New York. https://doi.org/10.1007/978-1-4612-1066-5_4

Puura, V. and Huhma, H. 1993. Palaeoproterozoic age of the East Baltic granulitic crust. *Precambrian Research*, **64**(1–4), 289–294. https://doi.org/10.1016/0301-9268(93)90082-D

Puura, V., Vaher, R., Klein, V., Koppelmaa, H., Niin, M., Vanamb, V. and Kirs, J. 1983. Кристаллический фундамент Эстонии (*The Crystalline Basement of Estonian Territory*). Nauka, Moscow.

Puura, V., Hints, R., Huhma, H., Klein, V., Konsa, M., Kuldkepp, R. et al. 2004. Svecofennian metamorphic zones in the basement of Estonia. *Proceedings of the Estonian Academy of Sciences, Geology*, **53**(3), 190–209. https://doi.org/10.3176/geol.2004.3.04

Rämö, O. T., Turkki, V., Mänttäri, I., Heinonen, A., Larjamo, K. and Lahaye, Y. 2014. Age and isotopic fingerprints of some plutonic rocks in the Wiborg rapakivi granite batholith with special reference to the dark wiborgite of the Ristisaari Island. *Bulletin of the Geological Society of Finland*, **86**, 71–91. https://doi.org/10.17741/bgsf/86.2.002

Rasilainen, K., Lahtinen, R. and Bornhorst, T. J. 2007. *The Rock Geochemical Database of Finland: Manual*. Geological Survey of Finland, Espoo.

Roser, B. P. and Korsch, R. J. 1986. Determination of tectonic setting of sandstone-mudstone suites using SiO_2 content and K_2O/Na_2O ratio. *The Journal of Geology*, **94**(5), 635–650. https://doi.org/10.1086/629071

Roser, B. P. and Korsch, R. J. 1988. Provenance signatures of sandstone-mudstone suites determined using discriminant function analysis of major-element data. *Chemical Geology*, **67**(1–2), 119–139. http://dx.doi.org/10.1016/0009-2541(88)90010-1

Rudnick, R. L. and Gao, S. 2003. Composition of the continental crust. In *Treatise on Geochemistry*, Vol. 3 (Holland, H. D. and Turekian, K. K., eds). Elsevier, Amsterdam, 1–64. https://doi.org/10.1016/B0-08-043751-6/03016-4

Saccani, E. 2015. A new method of discriminating different types of post-Archean ophiolitic basalts and their tectonic significance using Th-Nb and Ce-Dy-Yb systematics. *Geoscience Frontiers*, **6**(4), 481–501. https://doi.org/10.1016/j.gsf.2014.03.006

Saccani, E., Delavari, M., Dolati, A., Marroni, M., Pandolfi, L., Chiari, M. and Barbero, E. 2018. New insights into the geodynamics of Neo-Tethys in the Makran area: evidence from age and petrology of ophiolites from the Coloured Mélange Complex (SE Iran). *Gondwana Research*, **62**, 306–327. https://doi.org/10.1016/j.gr.2017.07.013

Shand, S. J. 1943. *Eruptive Rocks: Their Genesis, Composition, and Classification, with a Chapter on Meteorites*. John Wiley & Sons, New York.

Sifeta, K., Roser, B. P. and Kimura, J.-I. 2005. Geochemistry, provenance, and tectonic setting of Neoproterozoic metavolcanic and metasedimentary units, Werri area, northern Ethiopia. *Journal of African Earth Sciences*, **41**(3), 212–234. https://doi.org/10.1016/j.jafrearsci.2005.04.004

Skridlaite, G. and Motuza, G. 2001. Precambrian domains in Lithuania: evidence of terrane tectonics. *Tectonophysics*, **339**(1–2), 113–133. https://doi.org/10.1016/S0040-1951(01)00035-X

Skridlaite, G., Willingshofer, E. and Stephenson, R. 2003. P–T–t modelling of Proterozoic terranes in Lithuania: geodynamic implications for accretion of southwestern Fennoscandia. *GFF*, **125**(4), 201–211. https://doi.org/10.1080/11035890301254201

Soesoo, A. and Hade, S. 2012. Geochemistry and age of some A-type granitoid rocks of Estonia. In *Lithosphere 2012: Seventh Symposium on the Structure, Composition and Evolution of the Lithosphere in Finland, Espoo, Finland, 6–8 November 2012* (Kukkonen, I., Kosonen, E., Oinonen, K., Eklund, O., Korja, A., Korja, T. et al., eds). Institute of Seismology, Helsinki, 97–100.

Soesoo, A., Puura, V., Kirs, J., Petersell, V., Niin, M. and All, T. 2004. Outlines of the Precambrian basement of Estonia. *Proceedings of the Estonian Academy of Sciences, Geology*, **53**(3), 149–164. https://doi.org/10.3176/geol.2004.3.02

Soesoo, A., Košler, J. and Kuldkepp, R. 2006. Age and geochemical constraints for partial melting of granulites in Estonia. *Mineralogy and Petrology*, **86**, 277–300. https://doi.org/10.1007/s00710-005-0110-8

Soesoo, A., Nirgi, S. and Plado, J. 2020. The evolution of the Estonian Precambrian basement: geological, geophysical and geochronological constraints. *Proceedings of the Karelian Research Centre of the Russian Academy of Sciences*, **2**, 18–33. https://doi.org/10.17076/geo1185

Solano-Acosta, J. D., Soesoo, A. and Hints, R. 2023. New insights of the crustal structure across Estonia using satellite potential fields derived from WGM-2012 gravity data and EMAG2v3 magnetic data. *Tectonophysics*, **846**, 229656. https://doi.org/10.1016/j.tecto.2022.229656

Stephens, M. B. and Weihed, J. B. 2020. Sweden: lithotectonic framework, tectonic evolution and mineral resources. *Geological Society, London, Memoirs*, **50**. https://doi.org/10.1144/M50

Sun, S. S. and McDonough, W. F. 1989. Chemical and isotopic systematics of oceanic basalts: implications for mantle composition and processes. *Geological Society, London, Special Publications*, **42**(1), 313–345. https://doi.org/10.1144/GSL.SP.1989.042.01.19

Taylor, S. R. and McLennan, S. M. 1985. *The Continental Crust: Its Composition and Evolution*. Blackwell Scientific Publications, Oxford.

Verma, S. P. and Armstrong-Altrin, J. S. 2013. New multi-dimensional diagrams for tectonic discrimination of siliciclastic sediments and their application to Precambrian basins. *Chemical Geology*, **355**, 117–133. https://doi.org/10.1016/j.chemgeo.2013.07.014

Wan, L., Zeng, Z., Kusky, T., Asimow, P., He, C., Liu, Y. et al. 2019. Geochemistry of middle-late Mesozoic mafic intrusions in the eastern North China Craton: new insights on lithospheric thinning and decratonization. *Gondwana Research*, **73**, 153–174. https://doi.org/10.1016/j.gr.2019.04.004

Wood, D. A. 1980. The application of a Th–Hf–Ta diagram to problems of tectonomagmatic classification and to establishing the nature of crustal contamination of basaltic lavas of the British Tertiary Volcanic Province. *Earth and Planetary Science Letters*, **50**(1), 11–30. https://doi.org/10.1016/0012-821X(80)90116-8

Yang, G., Li, Y., Xiao, W., Sun, Y. and Tong, L. 2014. Petrogenesis and tectonic implications of the middle Silurian volcanic rocks in northern West Junggar, NW China. *International Geology Review*, **56**(7), 869–884. https://doi.org/10.1080/00206814.2014.905214

Paleoproterosoikumi metasetendite ja metavulkaniitide geokeemia, päritolu ja tektooniline asend Alutaguse piirkonnas

Juan David Solano-Acosta, Alvar Soesoo ja Rutt Hints

Uuring keskendub Alutaguse piirkonna Paleoproterosoikumi metasetendite ja metavulkaniitide kogukivimiproovide keemilistele analüüsidele, et mõista idapoolse Fennoskandia ala geodünaamilist arengut Svekofennia orogeneesi perioodil. Uuritud metasetendite üksused koosnevad vilgugneissidest (± Grt ± Crd ± Sil), metavulkaniidid aga peamiselt amfiboliitidest ja pürokseengneissidest. Töös on kasutatud nii ajaloolisi kui ka uusi kogukivimi koostise keemilisi andmeid. Leitud murenemisindeksid näitavad uuringuala kivimite sobivust setete päritolu ja tektoonilise asendi analüüsideks. Metasetendid on uuringus klassifitseeritud ränisisalduse järgi. Suure SiO_2-sisaldusega (>63 mass%) metasetendid sarnanevad litoklastilistele areniitidele, mis viitab suuremale küpsusele ja happelisele lähtematerjalile. Väikse SiO_2-sisaldusega (<63 mass%) metasetendite koostis sarnaneb grauvakkide ja savide omaga ning osutab pigem aluselise või keskmise koostisega lähtematerjalile. Tektoonilise diskriminantanalüüsi alusel saab metasetendeid seostada mandrilise riftistumisega. Alutaguse piirkonna metavulkaniidid klassifitseeruvad TAS-diagrammi alusel subleeliselisteks üksusteks. La/Yb *vs*. Zr/Nb ja La/Sm *vs*. Sm/Yb suhete põhjal on nende koostis kõige lähedasem primitiivse vahevöö omale. Th/Nb ja Th/Zr suhted viitavad basaltse lähtemagma seotusele astenosfääriga, samas kui Y/15–La/10–Nb/8 ja TiO_2–10(MnO)–10(P_2O_5) suhetest tuletatud metavulkaniitide geokeemiline signaal viitab lähtemagma vulkaaniliste saarkaarte päritolule. Oletatavalt võis Alutaguse struktuurne vöönd kujuneda Tallinna–Uusimaa vööndi(te) saarkaartetaguse basseinina pärast Bergslageni mikrokontinendi akretsiooni, 1,90–1,87 miljardit aastat tagasi, lõpetades Paleosvekofennia ookeani sulgumise.